JET-P(95)55

H-Mode Power Threshold Database for ITER

F Ryter and the H-Mode Database Working Group*

Max-Planck-Institut für Plasmaphysik, Euratom Association, D-85748 Garching, Germany.

*D J Campbell, T N Carlstrom[5], J P Christiansen, J G Cordey, J C DeBoo[5], S J Fielding[4], T Fukuda[7], R S Granetz[1], M Greenwald[1], Y Kamada[7], O J W F Kardaun[2], S M Kaye[8], J Kollermeyer[3], A Kus[2], T Matsuda[6,7], Y Miura[6], M Mori[6], E Righi, F Ryter[2,3], M Sato[7], D P Schissel[5], J A Snipes[1], U Stroth[2], A Suzuki[6], T Takizuka[7], H Tamai[6], K Thomsen, K Tsuchiya[7], M Valovic[4].

JET Joint Undertaking, Abingdon, Oxfordshire, OX14 3EA, UK.

[1] Alcator C-mod
[2] ASDEX
[3] ASDEX Upgrade
[4] Compass-D
[5] DIII-D
[6] JFT-2M
[7] JT-60U
[8] PBX-M

Preprint of a Paper to be submitted for publication in Nuclear Fusion

November 1995

H-MODE POWER THRESHOLD DATABASE FOR ITER

F. Ryter and the H-Mode Database Working Group*

Max-Planck-Institut für Plasmaphysik, EURATOM Association, D-85748 Garching

from Alcator- C-Mod: J. A. Snipes, R. S. Granetz, M. Greenwald
from ASDEX: O.J.W.F. Kardaun, A. Kus, F. Ryter, U. Stroth
from ASDEX Upgrade. F. Ryter, J. Kollermeyer
from COMPASS: S. J. Fielding, M. Valovič
from DIII-D: J.C. DeBoo, T. N. Carlstrom, D.P., Schissel
from JET: K. Thomsen, D.J. Campbell, J.P. Christiansen, J.G. Cordey, E. Righi
from JFT-2M: Y. Miura, N. Suzuki, M. Mori, T. Matsuda H. Tamai
from JT-60U: T. Fukuda, Y. Kamada, T Matsuda, M. Sato, T. Takizuka, K. Tsuchiya
from PBX-M: S.M. Kaye

DRAFT August 18 1995

Abstract

The ITER Threshold Database which presently includes data from 9 divertor tokamaks is described. The main results are presented and discussed. The features and dependencies of the power threshold in single devices are reviewed. In particular, the analysis shows a rather general linear dependence on magnetic field, but a non monotonic density dependence which varies from device to device. Investigation of the combined database suggests that the threshold dependence $P_{thres} \approx 0.3 NEL \times BT \times R^{2.5}$ *gives the best agreement with the data. This expression yields* $P_{thres} \approx 150$ *MW at a density of* $0.5\ 10^{20}$ m^{-3} *for ITER. Other expressions with weaker size dependence and therefore lower threshold power for ITER are also discussed. In addition the database is investigated by statistical discriminant analysis. The presently included edge data are described and discussed. A discussion with respect to ITER concludes this work.*

1. INTRODUCTION

The H-mode, an improved confinement regime obtained first in tokamaks [1] and more recently in stellarators [2], is a promising possibility for fusion reactors. The H-mode is reached above a certain threshold power which depends on plasma parameters and on the device. Since the discovery of the H-mode, efforts have been made to determine the power threshold dependence on plasma parameters in single machines [3-6]. It is, however, essential to be able to predict the H-mode operational window in the next generation of large tokamaks such as ITER and in particular the power necessary to reach the H-mode. This can be achieved at least along two ways: by empirically determining an expression for the power threshold dependence on global plasma parameters, or by identifying the physical parameters which control the H-mode transition. In both cases a database containing data from different devices is required to determine the size dependence. The L-to-H transition physics has been extensively studied in many tokamaks, as reviewed, for instance, in [7,8]. The fundamental observation is that the L-to-H transition happens at the plasma edge, just inside the separatrix. The electron and/or ion temperature or pressure (or their gradients) are believed to be determining physical parameters of the H-mode phenomena. This consideration guided the choice of the variables to be included in the threshold database as well as the analysis described in this paper. The constitution of the database means that both the following objectives can be pursued: 1) to predict the minimum

heating power necessary to reach the H-mode in future devices as a function of geometrical and physical parameters; 2) to contribute to physics studies of the L-to-H transition.

Using its existing infra-structure and the experience gained with the confinement database work [9,10], the "H-Mode Database Working Group" started in 1992 to gather H-mode threshold data from five divertor tokamaks (ASDEX, DIII-D, JET, JFT- 2M, PBX-M), and constructed an H-mode power threshold database. First results were presented in references [11,12]. The database was appreciably improved and extended in 1994 and 1995 with new data from the above devices, showing a lower threshold power, in particular due to boronization, and with data from new contributors: Alcator C-Mod [13], ASDEX Upgrade, COMPASS-D and JT-60U. This version of the database yields a lower threshold prediction for ITER than the first ones given in references [11,12].

This paper describes the present version of the ITER H-mode power threshold database, identified as ITERTH.DB1, as well as the essential results obtained by the "H-Mode Database Working Group". Its aim is to facilitate studies of this database by non-members of the group. The database was released in September 1995 and the way to access it is described in Appendix 3. The paper is structured as follows: the database is described in Section 2. Sections 3 and 4 describe the results from graphical analysis and exploratory data analysis with global parameters, applied to the single devices and to the combined dataset, respectively. Section 5 presents the results given by discriminant analysis. In Section 6, preliminary results obtained with edge data are discussed. Finally, Section 7 is dedicated to the discussion and conclusions. In this paper, we report observations made in single devices and generally indicate the corresponding reference. During the numerous discussions necessary for this work, experimental observations made in the different devices were reported by their representatives. Therefore, occasionally, experimental statements are made in this work without reference but with the agreement of the contributing group.

2. DESCRIPTION OF THE POWER THRESHOLD DATABASE

The threshold database contains 143 variables listed and defined in Appendix 1. This list is largely self-explanatory: the units are mks, temperatures are in eV and the geometrical parameters are defined in Fig. 1. The variable names of Appendix 1 are used in this paper and written in CAPITAL letters. The variables describe the plasma and are expected to give information on the H-mode transition physics. To the variables characterizing the plasma core, which are identical to those of the confinement database, [9,10], variables thought to be relevant for H-mode threshold and transition physics have been added. These are: 1) several separatrix-vessel distances, 2) an improved description of the magnetic configuration, 3) physical edge parameters at R95 such as density, temperature and edge radiation. Additional information on the H-mode transition and on the H-phase following the transition has been included. Finally, following the ITER needs, the structure of the database was recently modified and extended to allow studies of the H-to-L transition. We give in Appendix 2 the "reduced variable list", a subset of 20 variables absolutely necessary for the analysis presented in this work. This short variable list may be used for quick and easy contribution to the database, allowing simple analyses using global variables.

Two approaches have been used to assemble the database: 1) to take data from systematic parameter scans specifically made for threshold studies (identified by flags under variable ISEQ); or 2) to select data from L and H discharges covering the operational H-mode window of the devices. The L points are essential for discriminant analysis and, in some cases, to sort out the L and H regions without ambiguities. For the discharges achieving the H-mode, most

of the time slices were chosen in the L-phase just before the L-to-H transition (0.1 - 0.01 s), and shortly after the L-to-H transition (0.01 -0.2s). The PHASE variable defines the state of the plasma for the corresponding time slice, according to the definition given in Appendix 1. Some time slices have been taken later in the H-phase for additional studies. For the discharges not specifically dedicated to threshold studies (a majority in some devices) the heating power was abruptly turned on up to levels clearly in excess of the actual threshold. This problem will be discussed in a later section.

The database now includes 9 divertor tokamaks (Alcator C-Mod, ASDEX, ASDEX Upgrade, COMPASS-D, DIII-D, JET, JFT-2M, JT-60U and PBX-M), with various magnetic geometry and technical divertor features. The possible influence of the differences will be discussed in section 6. The present version of the database contains around 3800 time slices with Ohmic, NBI, ICRF, ECRH and LHCD heating, as defined by the AUXHEAT variable and distributed according to Table I. The main plasma parameter ranges covered in the database for each device are given in Tables II and III. One sees that RGEO varies by a factor of 6 between COMPASS-D and JT-60U, the plasma surface area by a factor of 30. Except ASDEX, all the devices have elongated cross-section with KAPPA between 1.4 and 1.9. BT varies in single devices by a factor of 2 to 3. Alcator C-Mod has the largest BT, NEL and NEL×BT values. The plasma facing components and wall conditions, known to influence the power threshold, are listed in table IV for the different devices. Their effects on power threshold, which are difficult to quantify, will be discussed in the next section. Finally, the time evolution of the discharges is recorded in a review sheet made for each shot. Typical examples are given in Fig.2 to Fig.5. A complete set of these review sheets is available for inspection at each participating laboratory and for some devices on the World Wide Web as described in Appendix 3.

3. OVERVIEW OF THRESHOLD FEATURES IN SINGLE DEVICES

The analysis is performed in a way similar to that sometimes used in confinement studies: 1) identify the key parameters in each machine and their dependencies, and find those common to all the devices (this section); 2) combine the data to determine the inter-machine dependencies (Sect. 4). In the present Section, we present an overview of the data provided by the different devices and we identify the essential conditions and parameters influencing the power threshold. We also analyse the data of the single machines to find common dependencies. The database includes a selection variable (SELDB1) based on a set of 10 criteria described in detail in Appendix 1. If all the criteria are fulfilled (SELBD1 = 1111111111), the conditions of the discharge fulfil the "standard criteria" and the corresponding time slice is assumed to represent a lower value of the threshold. Thus, the data from the different devices with SELBD1 = 1111111111 give a consistent dataset which is believed to yield the lower boundary of the threshold for each device for the data included in the database. The determination of the criteria is described in the following sub-sections. Note that SELDB1 will change when new data showing a lower threshold will be added to the database.

In the following, the threshold power, P_{thres}, is studied by using the total heating power absorbed by the plasma, P_{tot} = POHM + PABS - PFLOSS + P_{RF}, where PABS is the absorbed NBI power, PFLOSS are fast ions losses and P_{RF} is the heating power of any RF heating method. For reasons discussed later, $P_L = P_{tot}$ - dW/dt will be preferred when dW/dt is available which is generally the case for all the devices except for ASDEX Upgrade, COMPASS-D and DIII-D. For these devices P_L and P_{tot} are similar because, in these threshold experiments, the power steps were small. The threshold is defined here as the boundary separating the L and H mode regions, without any criteria on confinement time. In this approach, the dithering

H-mode (PHASE = D) is considered to be right at the threshold power and it is experimentally observed in the threshold investigations that the dithering H-mode is replaced by an actual H-mode (ELMing or not), with the corresponding confinement improvement, at powers ~10% higher than P_{thres}. This sharp transition between the L and H mode confinement can be attributed to the bifurcation character of the L-to-H transition and to the fact that the H-to-L transition occurs at powers significantly lower than P_{thres}, a phenomenon known as the H-mode hysteresis. In the whole paper, the data reported in the figures are taken from time slices just before the L-to-H transition or dithering, except where L-mode is explicitly specified. A low threshold power is obviously desirable for future devices and we will characterise a threshold feature as "favourable" if it reduces the threshold power.

Earlier studies in single machines [3–6,14,15], more recently confirmed in [12,16–18], showed that elements such as ion gradB drift direction, isotope of the target plasma, wall conditions and distances to the vessel also influence the threshold power. These features are now well established and will only be illustrated here with some examples. These studies also indicated almost no dependence of the threshold power on plasma current, an approximately linear dependence on toroidal magnetic field, BT, and to a lesser extent an also linear dependence on line-averaged density, NEL, at least above a certain minimum. Instructive H-mode existence diagrams were obtained by plotting the heating power versus the product NEL×BT and we will also use them to present the data. These observations guided the analyses made with the database and the NEL and BT dependencies are studied in the last two paragraphs of this section. Overview plots of the data included in the database are given for each device in Fig.6 to Fig.14. These figures show the BT, NEL and P_{tot} ranges for the standard selection in which the restriction criteria on low density (see section 3.8 and ISELDB1 in Appendix 1) was relaxed and for time slices just before the L-to-H transition. We adopted in these figures and for the whole paper the convention that BT is positive for the ion gradB drift direction towards the X-point (favourable direction). In these figures the data used later in the combined threshold analysis are printed with closed symbols. Depending on the device, extra information included in the database is also shown such as L-mode data or points without boronization (open symbols are used for these points). The normalisation of the heating power by the plasma surface area, S, (SPLASMA), motivated by the fact that the H-mode transition is occurring at the plasma edge, is simple and useful for comparisons between devices. Therefore we also present in Fig.6 - 14 P_{tot}/S versus NEL×BT existence diagrams for each device, although such a representation is not dimensionally correct, as discussed in section 5. Note that the threshold powers for the devices included in the database, which cover more than one order of magnitude, are brought together within a factor of 2 to 3 by this normalization.

3.1. Ion gradB drift direction, target gas isotope and heating method

The observation made earlier [3] that the power threshold is clearly lower for SN configuration with the ion gradB drift towards the X-point (favourable configuration), as compared to DN or SN with the opposite ion gradB drift, and confirmed later [5,6,14,15,17,19] is now established. This feature is illustrated here with data from JET in Fig. 15. Note that PBX-M only operates in the DN configuration, but all the other devices provided data with the favourable configuration. It is also now well-known that deuterium target plasmas show a 1.8 - 2 times lower threshold than hydrogen ones [3,5,14,19]. This property is illustrated in Fig.16 with data from JFT-2M. Results from DIII-D [20] (Ohmic, NBI) and recently ASDEX Upgrade [21] (Ohmic, ICRF and NBI) already showed that the method of heating does not basically influence the threshold value. Data from Alcator C-Mod (Ohmic and ICRF) and JET (NBI, ICRF) included in the database illustrate this point in Fig.17 and Fig.18. The available JET

data only allow the comparison between heating methods for DN and SN with unfavourable ion gradB drift. In summary, SELDB1 requires the favourable ion gradB direction (IGRADB=1, except for PBX-M), deuterium target gas, but there is no restriction on the heating method.

3.2. Wall conditions and divertor features

Wall conditions with low recycling (He glow discharge, boronization) clearly provide a lower threshold power. The majority of the devices included in the database now provided data from boronized discharges, except Alcator C-Mod which has molybdenum plasma facing components, JFT-2M which extensively performed Ti-gettering and JET which provided data with Be evaporation. The effect of boronization on threshold is particularly striking for DIII-D , JT-60U and PBX-M (Fig.10, 13, 14 respectively) in which the threshold power significantly dropped after boronization. Similar effects of smaller amplitude have been observed in several other devices. No difference is found in JET with or without Be evaporation. Wall conditioning and coating affect the impurity content but also recycling and neutral density, in particular at the plasma edge. Therefore the influence on threshold conditions may be attributed to the neutrals and is also linked to the retention properties of the divertor. In this respect, it is interesting to notice that for ASDEX, the threshold power was higher by a factor of 2 for the geometrically open divertor (large by-passes between main chamber and divertor) compared to the closed one, both cases without boronization [22]. These data are not included in the present database. For the geometrically closed ASDEX divertor (good retention of neutrals) the effect of boronization on threshold was small [14]. Fig.7 compares the threshold for two closed versions of the divertor, for the second version the vessel was boronized. They are very similar in the range NEL×BT $\approx$ 0.5 10^{20} m^{-3} T, but the first version with large divertor chamber provided a lower threshold at higher values of NEL×BT. This seems to be essentially due to a weak NEL dependence, but also to a weaker BT dependence of this version. These differences are not yet understood but illustrate the complexity of the threshold behaviour and the uncertainties due to effects not yet identified.

3.3. Plasma position and geometry

It is already well-known that the power required for the H-mode can significantly increase when the distance between plasma and machine structures becomes too small. The database shows this behaviour at least in JFT-2M for which the effect of the distance between separatrix and protection limiter, GAPOUT, is presented in Fig.19. Note the sensitivity of this effect which shows an e-folding length of the threshold increase of 1.5-2 cm, in agreement with SOL gradients in L-mode discharges and may be attributed to enhanced plasma wall interaction. Note also that at small values of GAPOUT, NEL increases, but not enough to keep P_L/NEL×BT constant, showing that other effects than NEL play a role, possibly the edge density or the neutral density. For ASDEX, similar effects have been observed but the corresponding data are not included in the database. The selection criteria requires the data to be restricted to discharges positioned "far enough from the wall" to avoid this influence, namely for ASDEX and JFT-2M GAPOUT $\geq$ 2.5 cm. The influence of plasma geometry on threshold is difficult to study because changing the plasma shape alters the divertor and plasma-wall interaction conditions. Data from the elongated tokamaks show the general trend that the threshold appears to decrease with elongation (KAPPA), but the KAPPA range available in the database for single devices is small and the magnitude of the dependence found using the available data strongly varies from device to device. This point is further investigated in section 5. As the elongation in ITER will be close to that of the devices represented in the database

this question is does seem to be of crucial importance.

3.4. Low q95 effects

ASDEX reported a strong increase of the power threshold on Q95 for values below 3 [14]. The present database also shows similar effects in JFT-2M and possibly in JET. This is attributed to stationary magnetic islands due to error fields causing perturbations of the edge plasma. This interpretation is supported by experiments with active error fields in JFT-2M [23]. Note that errors fields may increase the threshold due to changes in the edge plasma, e.g. ergodized regions, although mode locking does not occur. To avoid blurring our two-dimensional graphs, the condition Q95 $\geq$ 2.9 is applied to SELDB1 for these three devices. In the other devices this restriction is not necessary.

3.5. Fast ion effects in PBX-M

The NBI heating in PBX-M is provided by two pairs of neutral beam lines at different angles: "tangential" and "perpendicular". For the non-boronized dataset, the threshold power varies depending on whether the NBI is essentially perpendicular or tangential, perpendicular injection having the lower threshold. Fig.20 shows that the threshold values order well when plotted against the fast ion anisotropy, WFANI,: P_{tot}/NEL×BT decreases by more than a factor of 2 over the range included in the database. The restriction for SELDB1 is WFANI$\geq$0.55 for PBX-M. This restriction is consistent with the WFANI values of the other devices with NBI. The behaviour of P_{thres} with injection angle in PBX-M might be taken as an evidence of the favourable influence of edge ion losses on the L-to-H transition, in agreement with theoretical and experimental requirements of a negative electric field at the plasma edge [7,8].

3.6. Time constants affecting the threshold results

Assuming that the L-to-H transition occurs when the edge parameters have reached the necessary value under the influence of the heating power diffusing from the center towards the edge, the time constant to reach this state is of the order of one energy confinement time, τ_E, if the heating power is close to the actual threshold power. (Here the slowing down time of the fast ions is generally shorter than the confinement time). For discharges not specifically performed for threshold studies, the majority in some devices so far, heating powers well above the threshold were applied. In such cases, the plasma goes into the H-mode with a time delay (Δt = TIME - AUXTIME), after the heating turn-on (AUXTIME), which is short compared with τ_E. Clearly such experimental points are very high in the existence diagram. Therefore, if the lower points in the diagram are believed to represent the threshold, they must be achieved with low enough powers to be representative of the threshold. A selection criteria, $\Delta t \geq 0.5\tau_E$ was introduced to provide the possibility of selecting data for which the power is believed not to be far above the actual threshold. Note, however, that because they populate the H-mode region, points with powers clearly above the threshold are useful in some cases, for instance for discriminant analyses. Following the idea that the power must diffuse towards the edge, a better estimate of the threshold is probably obtained when the net power P_L is used instead of P_{tot}, at least for central heat deposition. This was done here depending on the possibilities available in the database. Fig.21 shows an example from JET where P/S×NEL×BT (P is either P_L or P_{tot}) is plotted versus the time delay Δt normalized to τ_E. In the region of short time delays, P_{tot} can be 3 times higher than for the long time delays. It is interesting to notice that in some cases for which the power is close to the threshold, time constants longer than τ_E

play a role, as indicated by transitions occurring after several confinement times. The reasons are not yet identified but such long time constants could be due to the evolution of recycling, wall conditions or current profile. Note also in Fig.21 the correction introduced when P_L is used instead of P_{tot}.

3.7. Magnetic field dependence

The magnetic field dependence of the threshold power, at constant density, is well documented in the database, except for the boronized JT-60U and in PBX-M for which the BT range is too narrow. The essential results are given in Fig.22. For this study the density was limited to narrow ranges indicated in the figures. A clear BT dependence appears in Alcator C-Mod ASDEX Upgrade, DIII-D, JET, JFT-2M, JT-60U (non-boronized) and a weak BT dependence is observed in COMPASS-D. Recent epxeriments at 8T in Alcator C-Mod [24] show the BT dependence in this device more clearly than the data presently in the database. The BT dependence in ASDEX was weak in the first divertor [3], but clear in the second divertor [14] as shown by the present data. In this respect it is also interesting to note that the threshold dependence on BT for limiter H-modes in JFT-2M is stronger than that observed for divertor H-modes.

3.8. Density dependence

The density dependence is more difficult to analyse than the BT dependence, it varies more from one device to the other and is more sensitive to the wall conditions, as shown for instance by the JT-60U data with and without boronization. In some cases the density range is too narrow to allow any statement on the NEL dependence. The results are given in Fig.23. In several devices the density dependence is not monotonic and the threshold power exhibits a minimum at NEL = NEL_{min}. This feature is not yet well documented in the database because this low density window was initially believed not to be essential. It was however reported in ASDEX [3], ASDEX Upgrade [21],and COMPASS-D [25] to be $NEL_{min} \approx 2.5\ 10^{19}\ m^{-3}$. For JFT-2M it is also well illustrated in the database (Fig.23). Alcator C-Mod reports $NEL_{min} \approx 8\ 10^{19}\ m^{-3}$, which is much higher than in the other tokamaks.

Below NEL_{min} the threshold power increases, in some cases sharply, with decreasing density and this region has not been studied in detail. In DIII-D this is attributed to the effects of locked modes which are becoming particularly sensitive at low density. For DIII-D only densities above $3.0\ 10^{19}\ m^{-3}$ were given to the database to avoid this problem. In JET, the NEL dependence at low values is complicated by a correlation with BT and Q95. Here P_{thres} seems to increase at low Q95. In Alcator C-Mod the existence of NEL_{min} is attributed to an operational low density limit specific to compact high field tokamaks occuring independently of the H-mode. This low density limit is characterized by the onset of run-away electrons. These electrons hit machine components and produce outgasing, as measured by pressure gauges which show a large increase of neutral gas pressure. The impossibility of achieving H-mode under these conditions is attributed to a strong threshold increase caused the high neutral pressure. Therefore, the particularly high value of NEL_{min} in Alcator C-Mod is probably a feature of compact high field tokamaks. In COMPASS-D, ASDEX Upgrade and JET the increase at low density is due neither to locked mode effects nor to particular effects and the threshold increase at low density gives indications on the L-to-H transition physics: for instance, the importance of the electron-ion coupling or of the penetration of neutrals.

The threshold increase at low density does not seem to be of determining importance for future large tokamaks, except if NEL_{min} increases with machine size or BT, for instance. Such

a behaviour is not supported by the available data, except by the high value of NEL_{min} in Alcator C-Mod which operates at BT = 5T. Encouraged by the ITER team, experiments are being foreseen in different devices to study NEL_{min} in more detail. The standard selection criteria requires NEL above NEL_{min}. The values of NEL_{min} are listed in Appendix 1, under variable SELDB1, as indicated by each device team.

Above NEL_{min}, which is the window we are interested in, a rather clear linear density dependence appears in Alcator C-Mod, ASDEX Upgrade, DIII-D, JET and PBX-M non-boronized. Due to the increase of the the radiated power at high density, the dependence on density in these devices is weakened if the radiated power is subtracted from P_{tot}. However, the present data do not allow a systematic study of this effect. JFT-2M and ASDEX show a weak density dependence, but the density range available possibly does not exceed NEL_{min} by much. The NEL dependence may also follow an off-set linear relationship in these machines. As the H-mode transition is occurring at the plasma edge, one expects the density to have an influence on power threshold. This effect is suggested in Alcator C-Mod with peaked profiles obtained after the injection of Li pellets [24].
The power threshold behaviour on density varies somewhat from device to device, it is non-monotonic but increases with increasing density above a certain density value. This topic is complex because it is related with operational limits, profile effects, neutral density, wall conditions and divertor properties.

4. POWER THRESHOLD FROM THE COMBINED DATABASE

The aim of the analysis of the combined database is to obtain the size dependence of the threshold. This study is guided by the observation that the H-Mode transition occurs at the plasma edge and that a given power flux through this plasma region is necessary to achieve the H-Mode. The power through a given surface of typical size R (R=RGEO) is written as: $P \sim R^2nTv$, where n, T and v are density, temperature and velocity across the surface. Assuming $v \sim \sqrt{T}$ yields $P \sim R^2nT^{3/2}$. A dimensionally correct form for the threshod power P_{thres} may be expressed as $P_{thres}=f(\rho^*,\nu^*,\beta,..)\times R^2nT^{3/2}$, where f is a function of dimensionless quantities such as $\rho^* \sim \sqrt{T}/RB$, $\nu^* \sim Rn/T^2$ and $\beta \sim nT/B^2$. We ignore mass effects, as here only deuterium plasma will be considered. If one assumes that only plasma physics phenomena determine the transition, which is a serious restriction at the plasma edge where atomic physics may also play a role and one neglects the physics occurring at the plasma frequency and on the Debye length scale, a threshold scaling which explicitly depends on engineering variables such as $P_{thres} \sim n^xB^yR^z$, and not on T, can be written as $P_{thres} \sim (\rho^*)^{\alpha_\rho}(\nu^*)^{\alpha_\nu}(\beta)^{\alpha_\beta}\times R^2nT^{3/2}$. This leads to the relation $1/2\alpha_\rho - 2\alpha_\nu + \alpha_\beta + 3/2 = 0$ and two further constraints are required to determine the exponents. These are suggested by the experimental observations, described in the previous section, as follows: 1) if the NEL×BT dependence observed in the single devices is correct then $P_{thres} \approx 0.3NEL\times BT\times R^{2.5}$ (corresponds to $\alpha_\rho = 0, \alpha_\nu = 1/2, \alpha_\beta = -1/2$); 2) if the BT×S dependence is correct then $P_{thres} \approx 0.016NEL^{0.75}BT\times S$ (corresponds to $\alpha_\rho = 1/2, \alpha_\nu = 1/2, \alpha_\beta = 3/4$); 3) if the NEL×S dependence is correct then $P_{thres} \approx 0.036NEL\times BT^{0.6}\times S$, (corresponds to $\alpha_\rho = 0.6, \alpha_\nu = 0.6, \alpha_\beta = -0.6$). Note that this approach does not give information on the aspect ratio and KAPPA dependence. The plots given by these expressions are presented in Fig.24. We also made the plot for the simple, but not dimensionally correct, $P_{thres} \approx 0.025NEL\times BT\times S$ relationship. As above, the threshold is assumed to be given by the lower boundary of the data points which is essentially determined by Alcator C-Mod, ASDEX Upgrade, DIII-D, JET, JFT-2M and in the best case JT-60U. Depending on the representation the three other devices are higher in the diagrams. For ASDEX this may

be due to the circular cross-section and for PBX-M due to the DN configuration. COMPASS-D deviates from the line determined by the larger tokamaks, but is aligned with the lower boundary of JFT-2M. It can only be speculated that this might reflect a change in the threshold behaviour for small devices at low magnetic field. The best agreement between the devices and a nicely linear lower boundary (except for COMPASS-D) is obtained with the $NEL \times BT \times R^{2.5}$ dependence. The other expressions lead to a larger scattering of the data and in particular to a bad agreement for JT-60U.

The extrapolation to the ITER EDA design gives about 150 MW for the $NEL \times BT \times R^{2.5}$ dependence, 65 MW for the $NEL^{0.75} BT \times S$ dependence, 60 MW for the $NEL \times BT^{0.6} \times S$ dependence and 85 MW for the $NEL \times BT \times S$ dependence, at a density of 0.5 10^{20} m^{-3}. These predictions for ITER vary by a factor of 2.5 and the expression showing the best agreement with the data yields the highest power. However, no definitive statement can be made from these results at present. A more reliable assessment of the BT and NEL dependencies in single devices, or a better understanding of the phenomena is required. It would also be important to better identify the cause of the scattering in the data. Divertor features and wall conditioning clearly play a role and may influence these results but these effects are quantified yet. In this context one of the possible candidates is the neutral gas pressure. Stimulated by the ITER team, threshold density studies are presently planned for several tokamaks to extend the range in NEL at different values of BT.

5. ESTIMATION OF POWER THRESHOLD SURFACE BY DISCRIMINANT ANALYSIS

Discriminant analysis is a method by which one can determine systematically an hyperplane or a quadratic surface on (natural) logarithmic scale in plasma parameter space that best separates two types of discharges, here L and H, given physically justified candidate plasma parameters [26–29]. In this section we present the results obtained with this method. They show, in some cases, differences with those from the previous sections. This is due to the fact that the dataset is extended in this section to include also low density discharges. Furthermore, the discriminant analysis yields the best separating hypersurface between the L and H regions, which does not necessarily corresponds to the lowest threshold considered in sections 3 and 4. The boundary given by the discriminant analysis is the surface above which about 50% of the shots included in this extended dataset went into the H-mode.

As for analysis of the energy confinement scaling, it makes sense to make a separate analysis per tokamak (without free geometrical exponents) before analysing the whole dataset. For this analysis an aggregated phase definition (PHASESEL) was used. We define as "L-mode for PHASESEL all values of PHASE that indicate essentially L-mode and as "H-mode for PHASESEL all values of PHASE that indicate essentially H-mode. Ohmic time slices were considered as L-mode. Dithering were omitted for reasons explained later in this section. The precise relation between PHASE and PHASESEL is given in table V. To avoid blurring by shots that are deep in the H-mode region, we also omitted PHASE=H in the analysis presented here. With PHASE=H included, the results are not dramatically different. Furthermore, we used the standard dataset selection relaxing the condition on the density (SELDB1= 1111111111 or 1111111011). For JT-60U, seven discharges with PHASE=DA are available in the database. Based on threshold experience for similar discharges in JT-60U [30], we constructed "virtual L-mode time slices at the same plasma parameters, but with lower power, P(L) = P(DA) - 1.5 MW for six of the seven discharges.

Although the basic H-mode physics parameters are probably provided by edge variables,

we consider here for simplicity the engineering variables P_{tot}/S, NEL and BT. The separating hyperplanes per tokamak are presented in Table VI. This table (similarly Tables VII and VIII) has to be read as: the best separating hyperplane is given by $c_{P_{tot}/S}\ln(P_{tot}/S) + c_{NEL}$ ln(NEL) + c_{BT}ln(BT) = c, or in the more usual power law form $P_{tot}/S \sim NEL^{a_{NEL}} BT^{a_{BT}}$. The errors (1 standard deviation) in the estimated coefficients $\hat{c}_i$ are also given in the Tables. The interpretation of the intercept, $\hat{c}$, is as follows: For $c > c_1 = \hat{c} + 0.2$, one is likely to get H-mode, for $c < c_2 = \hat{c}$ - 0.2, one is likely to stay in L-mode. For $c_1 < c < c_2$, one is in the intermediate region, where both L and H can occur. The value 0.2 has been chosen such that, as estimated from the dataset, for $c > c_1$, the specificity, i.e. the probability to allocate a shot (in the operating region of the dataset) as effectively L-mode, when it is indeed effectively L-mode is 95%, while the sensitivity, i.e. the probability to mislcassify an effectively H-mode shot, is about 50%.

In fact, one can construct the whole ROC (Receiver Operational Characteristic) curve, see e.g. [31], giving the sensitivity and specificity, or equivalently the probabilities of the two types of misclassification as a function of the constant c. The ROC curve represents the discriminating power of the procedure. The actual choice of the constant c depends on the (asymmetric) losses that are associated with the two types of misclassification. As it is more harmful to missclassify an L-mode shot than to misclassify an H-mode shot, it seems sensible to request a high specificity, as was done above. From a Bayesian interpretation, the posterior probability to get H-mode is 85% for $c > c_1$ and for a prior probability that is set equal the relative frequency of the H-mode in the sample (i.e. 55%).

It is noted that the separating hyperplanes have a direction which is roughly the average direction of the L-to-H and H-to-L transition surfaces, and that the above statement is only adequate under the assumption that those two surfaces are, in reasonable approximation, parallel to each other on logarithmic scale.

Table VI shows a rather clear BT dependence of the power threshold consistently across the tokamaks for which sufficient data are available to allow a separate analysis of P_{tot}/S against NEL and BT, but for NEL this is considerably less so. In fact, a similar analysis with a quadratic NEL dependence (on log scale) shows that JET and JFT-2M exhibit a significant positive curvature, indicating that the threshold power, as a function of the density, at constant BT, exhibits a minimum, as also discussed in section 3. The curvature is not significant for ASDEX and DIII-D boronized. For Alcator C-Mod and ASDEX Upgrade the curvature diminished and became not significant when the dithering phases were omitted because the dithering phase are at the lower end of the density window where the threshold increases with decreasing density. For the remaining tokamaks, the condition of the dataset did not allow to make a firm statement. This indicates that the dependence on density, which was taken instead of e.g. edge density or the neutral particle density, for reasons of diagnostic availability and easiness of engineering control, is more complicated than can be adequately described by a simple power law.

Nevertheless, if one merges the dataset and makes a joint discriminant analysis of P_{tot}/S against NEL, BT, R, A=R/AMIN, and KAPPA, one gets the result as presented in Table VII, which are relatively stable under moderate alterations of the standard dataset. A graphic representation of the data is shown in Fig.25 for the expression given in Table VII. The negative dependence on KAPPA is favourable for elongated devices and a lower aspect ratio also seems to be somewhat favourable to reduce the threshold. The size dependence of P_{thres} is given by $S \times R^{-1.23} = R^{0.77}$, which is clearly weaker than the results from the previous section. The low R dependence provides, on one hand the good agreement of COMPASS-D with the majority of the other tokamaks, on the other hand the poor agreement of JT-60U shown by Fig.25. The

BT dependence is in agreement with the other results. Under the -unjustified- assumption of a simple power law w.r.t. NEL, virtually no NEL dependence is found, which is not in agreement with the majority of the experimental results shown in Section 3.8. This might arise from the fact that the devices show different density dependencies (Fig.24) and cover different density windows, while also low density data were included in the discriminant analysis. Compared to the representations of section 4, one observes a good agreement of the lower boundary for most of the tokamaks except for Alcator C-Mod, due to the weak R and NEL dependencies. Note here the agreement of ASDEX (KAPPA = 1) with the elongated devices. Due to its low r dependence, the expression from Table VII predicts about 70 MW for ITER at NEL=0.5 10^{20} m^{-3}. It is speculated that the R dependence may possibly be related to the H-to-L transition plane having a more favourable R dependence than the L-to-H transition plane and possibly to the influence of the Ohmic data. This topic, however, requires further investigations.

To better take the density behaviour into account, the following quadratic interaction model (qm), on log scale, to the first order between density and plasma surface area was developed: $c_{P_{tot}/S}\ln(P_{tot}/S) + c_{S,qm}\ln S + c_{NEL,qm}\ln NEL + c_R \ln R + c_{BT}\ln BT + c_{IP}\ln IP = c$, or in the power form $P_{tot} \sim S^{a_{S,qm}} NEL^{a_{NEL,qm}} R^{a_R}\, BT^{a_{BT}} IP^{a_{IP}}$ The expressions for $a_{S,qm}$, $a_{NEL,qm}$ and the values of the other coefficients giving the best fit are given in Table VIII. In an initial study we allocated dithering phases as H-mode. This lead to complicated curvatures (i.e. higher order between NEL and S) of the discriminant surface which disappeared when the dithering phases were omitted. Therefore the results presented here were performed without dithering, according to table V. It must be stressed that the size dependence is now given by 3 factors, $S^{a_{S,qm}}$, $NEL^{a_{NEL,qm}}$ and R^{a_R}, and cannot be simply deduced from a_R. In particular, the quadratic term in S introduces a saturation of the size dependence for large devices, which is only partly compensated by $NEL^{a_{NEL,qm}}$. The effective R dependence with this model varies between $R^{1.5}$ and $R^{0.7}$ when going from COMPASS-D to JET for NEL = 0.5 10^{20} m^{-3}. The extrapolation to ITER yields $P_{thres} \approx 70$MW for NEL=0.5 10^{20} m^{-3}. It must be noted here that omitting the Ohmic points in the analysis, which modifies essentially the contributions from Alcator C-Mode and COMPASS-D, yields an expression for which the ITER prediction is about 50 MW higher. The dependencies on KAPPA and A disappear in this analysis. The significant Ip dependence found here is not in agreement with results obtained in section 4 and generally in single devices. The reason for this is not yet identified, but it reflect a dependence on Q95. This model gives a reduction of the RMSE which is significant according to the F-test at about the 1% level, in comparison with the simple power of Table VII.

The expression $a_{NEL,qm}$ aims at consistently treating the density for all the devices. It provides a non-linear dependence of P_{tot}/S as a function of NEL and S, with a minimum (NEL_{min}, as in section 3.8) inside the density range of most of the devices considered here. The values of NEL_{min} roughly correspond to the experimental observations mentioned in Section 3.8. The position of NEL_{min} decreases somewhat with S and the curvature of the threshold surface increases with S. The contribution of the density to threshold increases with S at NEL_{min}. The result obtained with this model is graphically represented in Fig.26. In spite of the quadratic term $S^{a_{S,qm}}$ included in the model, the agreement with the data is reasonable for all the devices, except COMPASS-D, as also shown by the results of Fig.24 from the previous section. To better fit this device, one probably should also take into account additional plasma parameters or divertor properties. New data from this device will perhaps help in understanding this point.

It seems worthwhile to pursue discriminant analyses also while taking additional variables into account, such as neutral density, edge density. These quantities are planed to be included in the database.

6. EDGE TEMPERATURE AND DENSITY

Because of the difficulties of performing systematic localized measurements at the plasma edge, the present database is rather incomplete for what concerns the edge variables. In this version of the database, edge electron temperature and density as well as ion temperature are available for JET. The electron temperature is from the ECE measurement and limited to BT values above 2T. Electron density and temperature are obtained from the single pulse Thomson scattering system for the DIII-D non-boronized subset, mainly in L phases and not always close to the transition. Two points in H-mode phases are given. The L-mode data (pre-transition time slices for JET), presented in Fig.27, show for both devices a well defined variation of NE95 with NEL, as expected in L-mode phases. The density profile in JET is somewhat broader than in DIII-D. Such a behaviour between edge and line-averaged density is expected in the L-mode for the other devices, as well as an increase of the density peaking with decreasing machine size. Therefore, threshold analyses similar to those presented in previous sections but made with the edge density if it were available, would not yield very different results, except in particular cases such as pellet injection.

The available edge data are further documented in Fig.28 and Fig.29. Fig.28 shows that TE95 is clearly larger in JET than in DIII-D before the L-to-H transition and that, due to the large scattering of TE95 in JET, no clear dependence can be recognised. Analyses show that TE95 is consistent with the averaged electron temperature and with the energy content. Therefore the scattering of TE95 cannot be fully attributed to that of the edge measurement. The coherent pattern of Fig.29 is logically due to the increase of NE95×TE95 with threshold power which increases with NEL×BT as shown in section 4. Consistently, the two DIII-D points taken in the H-mode, known to have high edge pressure, show higher values of NE95×TE95. The thin and clear separation between the DIII-D L-mode region and the JET pre-transition points is remarkable and may underline the role of edge pressure in L-to-H transition physics. However, looking for the parameter determining the threshold means that this parameter should be constant when plotted versus NEL×BT. The data shown here are in agreement with the earlier observation in DIII-D, [4,32], that T_e/BT is constant at the L-to-H transition, which might reflect the role of the Larmor ($\sim T_e^{0.5}$/BT) radius in transition physics. Within the precision of the present data, the distinction between the T_e and $T_e^{0.5}$ dependencies cannot be made. Other parameters constant at the transition could not be obtained with the present database. Some comments can be made though. The edge temperature certainly plays a key role for the L-to-H transition but it is not the unique parameter because it is expected to increase with power in the pre-transition L-phase and from device to device. The data also indicate that electron edge collisionality ($\sim n_e T_e^{-3/2}$) cannot be the unique criterion for the transition because this quantity varies by one order of magnitude between JET and DIII-D for the present data. Note that the variation of edge collisionality between the 9 devices included in the database is even larger. Finally, one should not forget that ions possibly also play an important role in the H-mode transition physics.

Being aware of the importance of collecting edge data both for physical understanding and for extrapolations, the tokamak groups participating in the database work have agreed to intensify their efforts to provide the database with edge data. It would be particularly convincing in BT scans made over a large range at constant density.

7. DISCUSSION AND CONCLUSION

The analyses performed with the present database show an overall agreement of the threshold features and dependencies between the 9 tokamaks, but also differences. In this section we discuss these results from the point of view of a future device like ITER. In this case one would like to choose the conditions providing a low threshold power and estimate the influence of the controllable parameters on its value. Low threshold power requires single-null configuration with the ion gradB drift directed towards the X-point, which is ITER's configuration. Deuterium plasmas are favourable for H-mode and at present one has no indication that the threshold would be higher in tritium. A lower threshold in tritium than in deuterium is possible, but not by more than 25%, assuming a linear decrease of P_{thres} with mass. The heating method, at least as long as it is centrally deposited, does not play a key role and one has no reason to expect alpha heating to be unfavourable for H-mode, at least in the density region where electrons and ions are not strongly decoupled. The threshold increases at high neutral density in the main chamber, which depends on divertor features and wall conditioning for given operating conditions. Due to their size and geometrical arrangement, the divertors of the devices included in the database have different features, in particular different neutral retention. With the present version of the database it is not yet possible to quantify this effect on threshold and on the extrapolation made for ITER. Neutral pressure measurements may be a way to quantify this somewhat and additional corresponding data will be included in the database. The new divertors which will be installed in several tokamaks in the near future (ASDEX Upgrade, DIII-D, JET, JFT-2M) are expected to improve the knowledge on this topic. The present divertor concept of ITER and the size of the device will provide good neutral retention and should be favourable for the H-mode. Wall conditioning for low recycling must be provided. Summarising, the basic criteria for a low threshold seem to be fulfilled in ITER.

It remains, however, to discuss the dependence on magnetic field, density, machine size and geometry. The BT dependence appears to be linear in the larger devices participating to the database and weaker or off-set linear in smaller devices. The value for BT in ITER will be less than two times that of the present larger devices (JET, JT-60U), whereas Alcator C-Mod provided data with weak BT dependence between 2.5T and 5T. As shown above, the threshold dependence on density is less clear and dedicated experiments are foreseen in several devices to address this question. However, the existing data, again from larger devices (ASDEX Upgrade, DIII-D, JET) show a rather clear linear dependence (above NEL_{min}), possibly somewhat stronger than linear for the upper part of the density window (above 0.6 10^{20} m^{-3}), possibly due to the strong gas puffing necessary to reach high density in the L-mode [33]. ASDEX and JFT-2M show a flatter dependence. It seems reasonable in ITER to be able to achieve the H-mode at moderate density (0.3 - 0.5 10^{20} m^{-3}) and use the good particle confinement observed in the H-mode to reach the necessary high density. Therefore, the crucial question for ITER is the behaviour of the H-to-L transition at high density, which was defined as an urgent ITER Task. A further question about the density is that of the low density threshold, NEL_{min}, for which, as already mentioned, data are still needed to allow a firm statement. If NEL_{min} is around 0.25 10^{20} m^{-3} in all the devices and is independent of plasma or machine parameters, it should not cause problems for ITER. However, if NEL_{min} increases with BT or machine size, ITER will not be able to take advantage of low threshold power at low density.

Concerning the threshold dependence on geometry, it should be noted that the plasma shape in ITER (elongation, triangularity) is similar to that of most of the devices included in the database and these parameters are not considered here. However, the results of sections 4

and 5 suggest that the threshold dependence on machine size lies between $R^{1.5}$ and $R^{2.5}$ and therefore extrapolation from JET to ITER yields factors of about 5 and 14 respectively. Thus, the machine size clearly causes the strongest increase of threshold power when extrapolating to ITER. For example, taking the threshold in JET (P_{thres} = 5 MW) at NEL = 0.5 10^{20} m^{-3} and BT = 3 T implies a threshold in ITER at the same density and BT = 6T between 50 MW and 150 MW for $R^{1.5}$ and $R^{2.5}$ respectively. Note, however, that R in ITER is only 2.6 to 2.8 times larger that those of JET and JT-60U, whereas in the database R varies by a factor of 6.

Other effects which may influence the threshold are briefly reviewed below. It was mentioned above that active or intrinsic error fields cause a higher threshold. This effect is not well documented so far and further studies are necessary to assess the extent to which intrinsic error fields could cause the H-mode to be high in ITER. Recent experiments in DIII-D with error field correction suggest that the effect could be important. Therefore, error field correction by active loops might be of importance in ITER. The losses of ripple trapped ions might also play a role in the H-mode transition and could increase or decrease the threshold depending on their properties. In this context, it is noticed that the ripple values of the tokamaks included in the database vary between 0.1% and 1% but no trend on threshold could be found. Recent experiments in JET showed a weak effect of ripple on threshold power in the range 0.1% to 2% [34].

The results from the discriminant analysis of the standard dataset, extended by the low density shot are as follows: In addition to the usual variables NEL, BT and machine size, a significant and unfavourable current dependence was found for JET as well as for the combined dataset, in opposition to the results found otherwise. Both in a simple power-law model for P_{thres} where the dependence on the current was neglected, as in a quadratic model (on log. scale) with interaction between NEL and BT, while including the current dependence, the size dependence of P_{thres} is more favourable then from the intuitive analysis aided by dimension considerations. In the latter case, there is, at constant IP, a signifiacnt saturation effect with S. Remarkably, the KAPPA and aspect ratio dependencies disappear when a quadratic model in S (and NEL) is used. The dependence on density exhibits a minimum which decreases slightly with machine size ($NEL_{min} \simeq 7/S^{0.2}$). No such interactions have been found between BT and S and between NEL and BT. Including the dithering data into the analysis led to nominally significant higher order interactions between NEL and S. Because of this, and since the dithering shots have been included mainly from a few machines (ASDEX Upgrade, Alcator C-Mod, JET), possibly with slightly different definitions, they were left out from the discriminant analysis presented. The results from the present discriminant analysis suggest a lower threshold power for ITER (around 70 MW for both the simple power law model and for the interaction model) than the threshold power based on the more intuitive analysis. So, from this point of view also, it seems worthwile to investigate this topic further.

It is a legitimate question to ask how the threshold could be (actively) reduced in ITER. Apparently the present possibilities are rather limited: apart from scenarios taking advantage of low density and tritium, one can think of active divertor biasing or applying RF in the Alfvén or Bernstein wave domain, or vertically injecting neutrals at the plasma edge to produce localized edge ion losses, but no convincing results exist so far. There is no doubt that the threshold has decreased since the discovery of the H-mode and that an important element in this evolution is the wall conditioning. Further improvement along this line might be possible. Finally, a better understanding of the phenomena causing and inhibiting H-mode may suggest the ways of actively and economically reducing the threshold. It also must be remembered that the H-to-L transition occurs at powers lower than P_{thres} which allows a significant increase in the density without quenching the H-mode. The dependencies of the H-to-L threshold have not

been studied carefully yet, but the database allows the analysis of this crucial question and the participating teams are making efforts to experimentally address this topic as defined in the ITER Task on threshold.

The H-mode is triggered by edge conditions and therefore edge measurements are most probably necessary to address the H-mode physics as discussed in the previous section. However, even if it were possible to provide a threshold prediction using the physical threshold edge parameters, this would not reduce the uncertainty for ITER, because presently no model is able to predict edge parameters in ITER with sufficient reliability.

In summary, prediction with global parameters is the best which can be done presently. The present database and analyses will be improved in the near future by the dedicated threshold studies being performed or scheduled to be performed in several devices. Edge data are necessary to improve the physical understanding and to suggest possibilities to reduce the threshold power.

ACKNOWLEDGEMENTS

The physics and diagnostic teams from the different devices are warmly thanked for providing the experimental data. The authors are grateful to the technical and operation groups for their excellent support. It is a pleasure to acknowledge fruitful discussions with K. Lackner and A. Bergmann on dimensionless considerations.

Alcator C-Mod work supported by U.S. Department of Energy Contract No DE-AC02-78ET51013. DIII-D work was supported at General Atomics by the U.S. under DOE Contract No. DE-AC03-89ER51114. A portion of the PBX-M work was supported under U.S. DOE Contract No DE-AC02-76-CHO-3073.

REFERENCES

References

[1] WAGNER, F. et al., Phys. Rev. Lett. **49** (1982) 1408.

[2] ERCKMANN, V. et al., Phys. Rev. Lett. **70** (1993) 2086.

[3] ASDEX team, Nucl. Fusion **29** (1989) 1959.

[4] BURRELL, K. H. et al., Plasma Phys. Controlled Fusion **31** (1989) 1649.

[5] JFT-2M group, presented by Y. Miura, Proc. 3^{rd} H-Mode Workshop **1** (1991) 141.

[6] NARDONE, C. et al., Proc. of the 18^{th} Europ. Conf. on Controlled Fusion and Plasma Heating, Berlin, Part. I **15C** (1991) 377.

[7] BURRELL, K. H. et al., Plasma Phys. Controlled Fusion **34** (1992) 1859.

[8] GROEBNER, R. J., Phys. Fluids B **7** (1993) 2343.

[9] CHRISTIANSEN, J. P. et al., Nucl. Fusion **32** (1992) 291.

[10] THOMSEN, K. et al., Nucl. Fusion **34** (1994) 131.

[11] H-Mode Database Working Group, presented by Kardaun O. J. W. F., Plasma Physics and Controlled Nuclear Fusion Research (Proc. 14^{th} Int. Conf., Würzburg, 1992), IAEA, Vienna, **3** (1993) 251.

[12] RYTER, F. et al., Controlled Fusion and Plasma Physics, Proceedings of the 20th European Conference, Lisbon, Part I **17C** (1993) 15.

[13] SNIPES, J. A. et al., Nucl. Fusion **34** (1994) 1039.

[14] RYTER, F. et al., Proc. of the 19^{th} Europ. Conf. on Controlled Fusion and Plasma Heating, Innsbruck, Part I **16C** (1992) 195.

[15] WARD, D. et al., Proc. of the 18^{st} Europ. Conf. on Controlled Fusion and Plasma Heating, Berlin, Part I **15C** (1991) 353.

[16] CARLSTROM, T. et al., Plasma Phys. Controlled Fusion **36 Suppl (7)A** (1994) A147.

[17] START, D. F. H. et al., Proc. of the 21^{st} Europ. Conf. on Controlled Fusion and Plasma Heating, Montpellier, Part I **18B** (1994) 314.

[18] RYTER, F. et al., Controlled Fusion and Plasma Physics, Proceedings of the 21th European Conference, Montpellier, Part I **18C** (1994) 334.

[19] LACKNER, K. et al., Plasma Phys. Controlled Fusion **36 Suppl (12)B** (1994) 79.

[20] OSBORNE, T. H. et al., Nucl. Fusion **30** (1990).

[21] RYTER, F. et al., Plasma Phys. Controlled Fusion **36 Suppl (7)A** (1994) A99.

[22] WAGNER, F. et al., Plasma Physics and Controlled Fusion Research (Proc. 13^{th} Int. Conf., Washington, 1990), IAEA, Vienna **1** (1991) 277.

[23] LEONARD, A. W. et al., Nucl. Fusion **31** (1989) 1511.

[24] TAKASE, Y. et al., Controlled Fusion and Plasma Physics, Proceedings of the 22th European Conference, Bornemouth", to be published (1995).

[25] FIELDING, S. J. et al., H-modes in iter-like configurations on compass-d tokamak, in *Plasma Physics and Controlled Fusion Research (Proc. 15^{th} Int. Conf., Seville, 1994, paper IAEA-CN-60/A-2/4-P-4, to be published).*

[26] MARDIA, K. V. et al., *Multivariate Analysis*, Academic Press, 1979.

[27] FLURY, B. et al., *Multivariate Statistics*, Chapman and Hall, 1988.

[28] KARDAUN, O. et al., Computational Statistics, Proc. 10th Symp. on Comp. Statistics I (1992) 163.

[29] KARDAUN, O. et al., Report NIFS 242 (1993).

[30] SATO, M. et al., H-mode of high toroidal field plasmas in JT-60U, in *Plasma Physics and Controlled Fusion Research (Proc. 15^{th} Int. Conf., Seville, 1994, paper IAEA-CN-60/A-2-II-4, to be published).*

[31] KARDAUN, J. et al., Meth. Inf. Med. **29** (1990) 12.

[32] CARLSTROM, T. N. et al., Proc. of the 16^{th} Europ. Conf. on Controlled Fusion and Plasma Heating, Venice **13B part I** (1989) 241.

[33] RIGHI, E. et al., Controlled Fusion and Plasma Physics, Proceedings of 22th European Conference, Bornemouth", to be published (1995).

[34] TUBBING, B. et al., Controlled Fusion and Plasma Physics, Proceedings of the 22th European Conference, Bornemouth", to be published (1995).

Figure caption

Fig.1: Definition of the plasma geometry variables

Fig.2 - 5: Example of review sheets for Alcator C-Mod, ASDEX Upgrade, COMPASS-D, JT-60U.

Fig.6 - 14: Overview plots for the data from the different tokamaks.

Fig.15: Influence of ion gradB drift in JET

Fig.16: Influence of isotope effect in JFT-2M

Fig.17 - 18: Comparison of heating method in Alcator C-mod and JET

Fig.19: Effect of plasma-wall distance in JFT-2M

Fig.20: Effect of fast beam ions in PBX-M

Fig.21: Effect of time delay in JET

Fig.22: BT dependence in the different devices

Fig.23: NEL dependence in the different devices

Fig.24: Results from the combined database

Fig.25: Results from the combined database with discriminant analysis

Fig.26: Results from the combined database with discriminant analysis using an inter-action model

Fig.27: NE95 versus NEL from DIII-D and JET

Fig.28: TE95 versus NEL×BT for DIII-D and JET

Fig.29: NE95×TE95 versus NEL×BT for DIII-D and JET

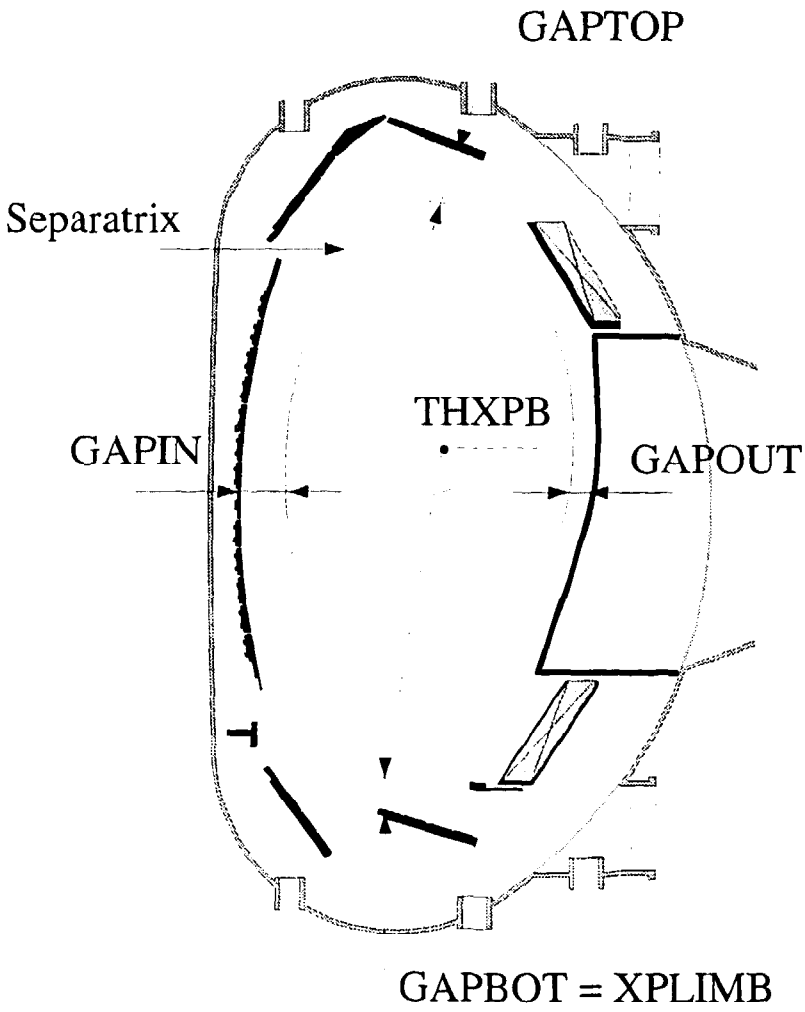

Fig.1 Cross-section of ASDEX Upgrade which illustrates the different distances (GAPs) between plasma and machine components available in the database.

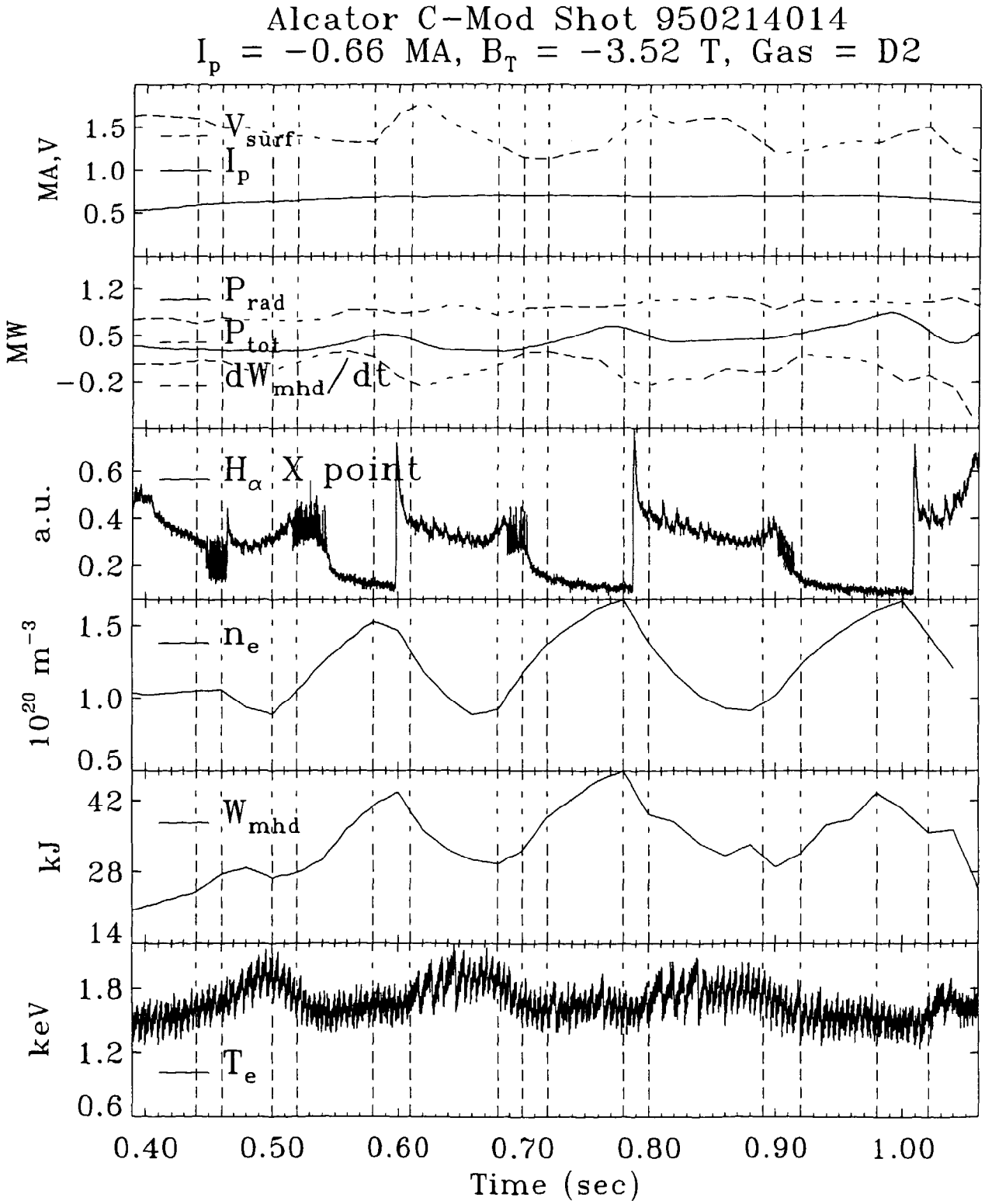

Fig.2 Example of a review sheet from Alcator C-Mod. The dotted lines indicate the time slices included in the database.

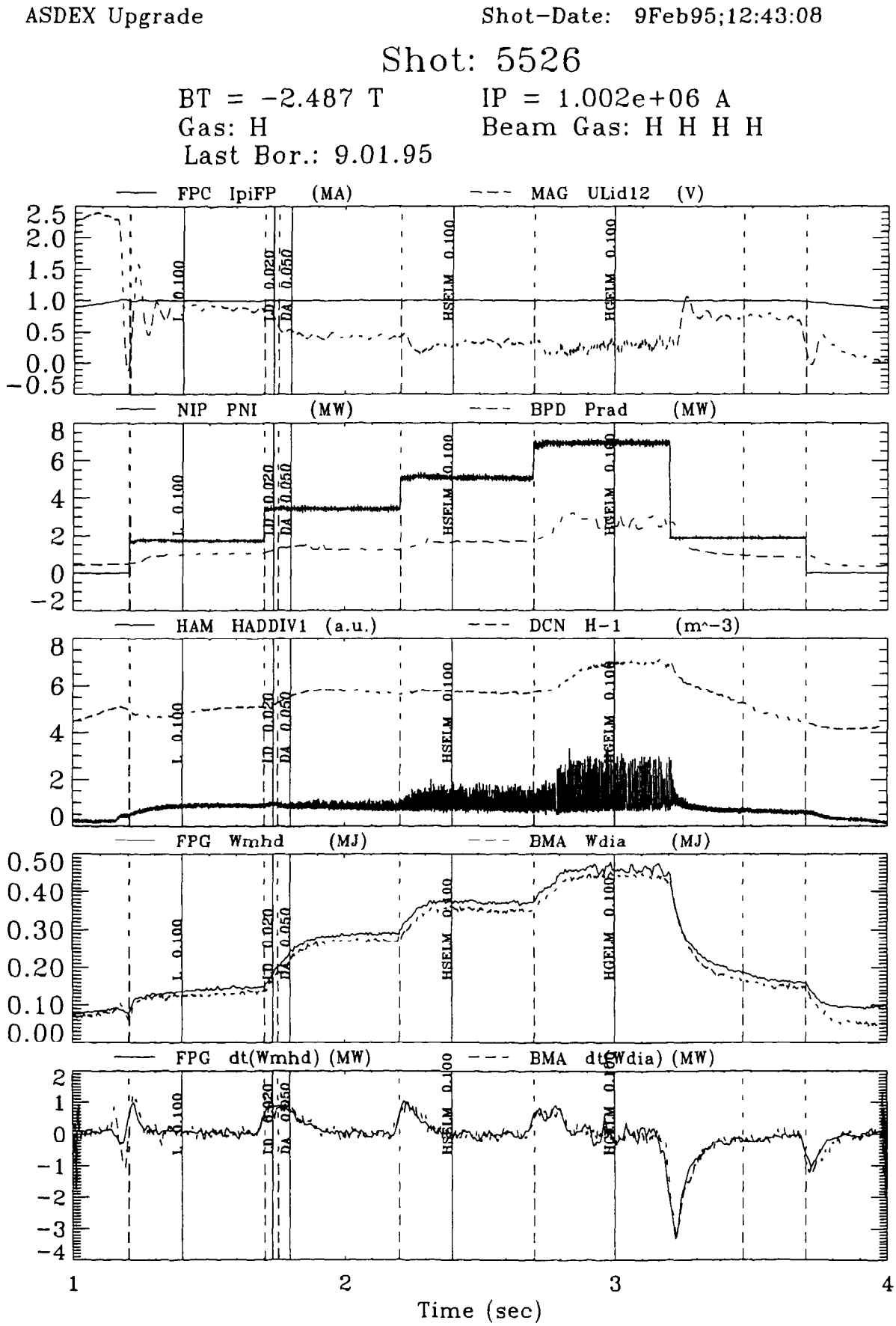

Fig.3 Example of a review sheet from ASDEX Upgrade. The solid lines show the position of the time slices. The phase definition and the smoothing time are written along each line. The dashed lines indicate the position of the LH and HL transitions, the dotted lines the position of AUXTIME.

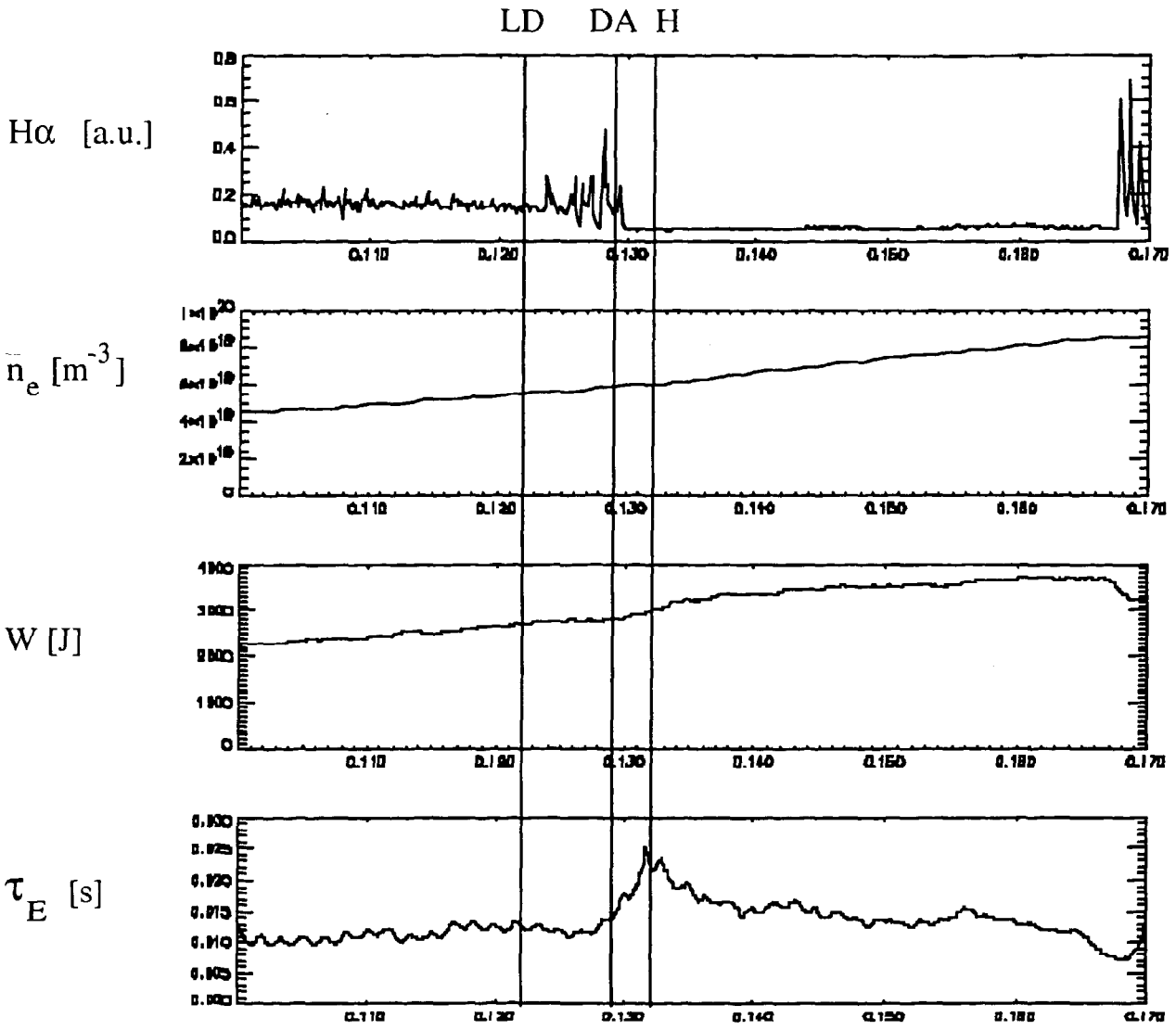

Fig.4 Example of a review sheet from COMPASS-D (shot 13130). The vertical lines denote the slected time slices. Hα is the emission from the outboard midplan.

Fig. 5 Review sheet from JT-60U

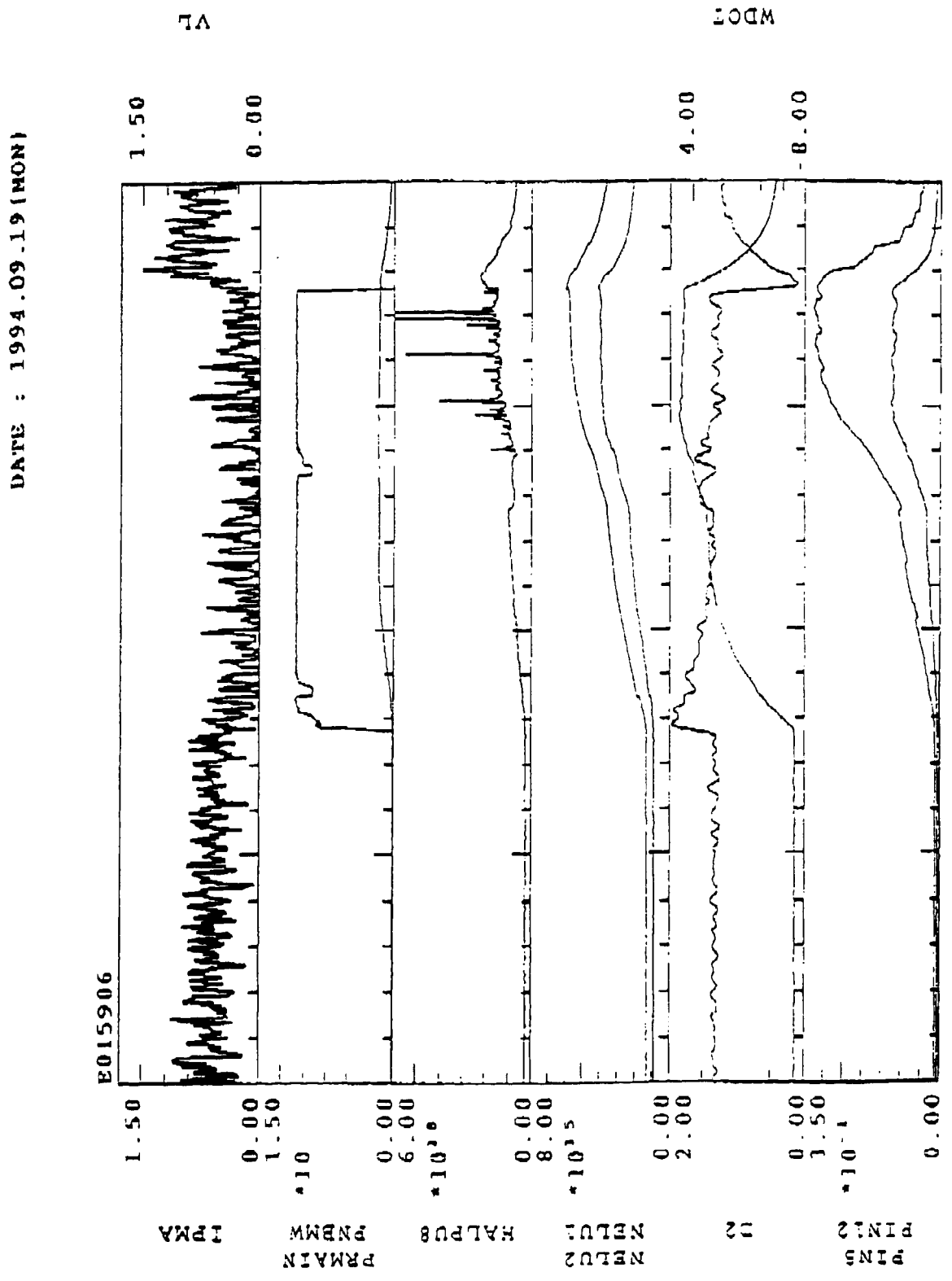

Fig.6: Alcator C-Mod overview plots. The symbols used in a and b correspond to different BT ranges directly shown in a. The symbols used in c and d are define in the figures.

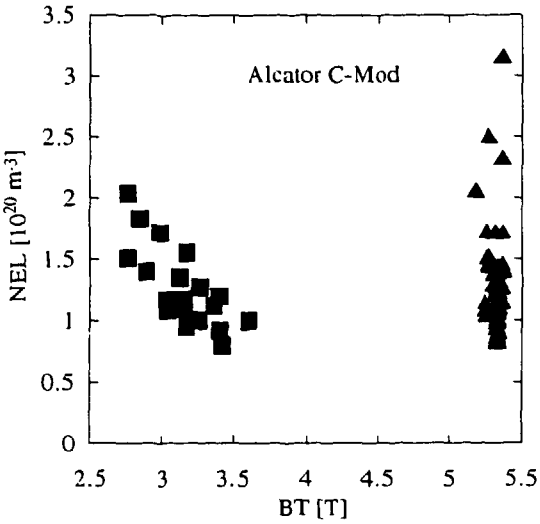

Fig. 6.a

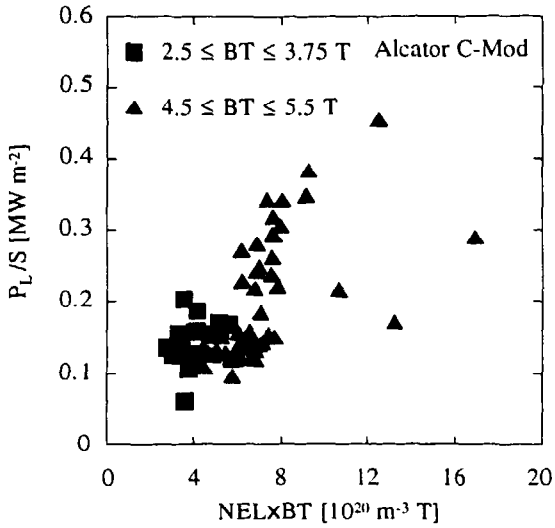

Fig.6.b

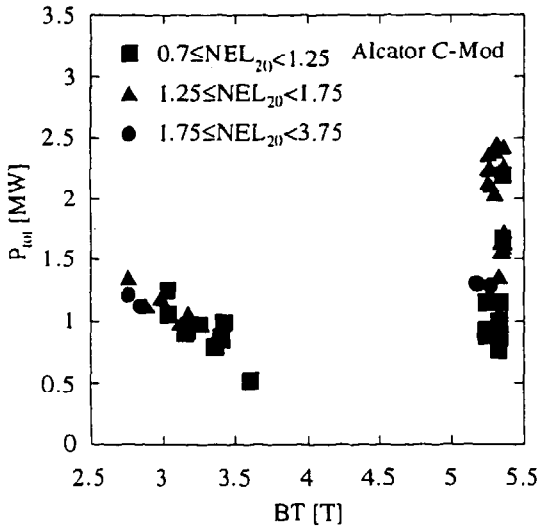

Fig.6.c

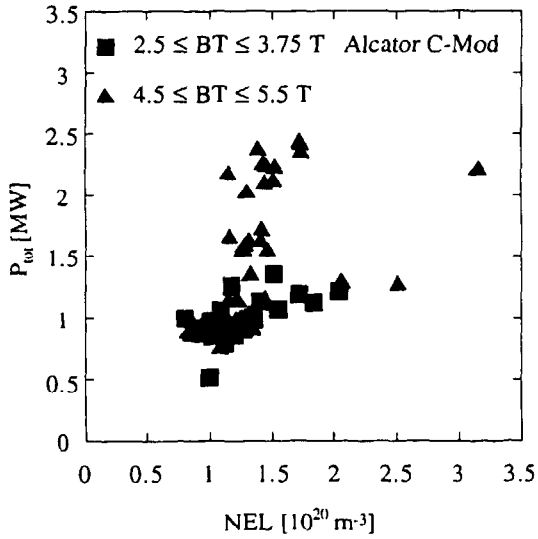

Fig6.d

Fig.7: ASDEX overview plots. The symbols used in a and b correspond to differer BT ranges directly shown in a. The symbols used in c and d are defined in the figures.

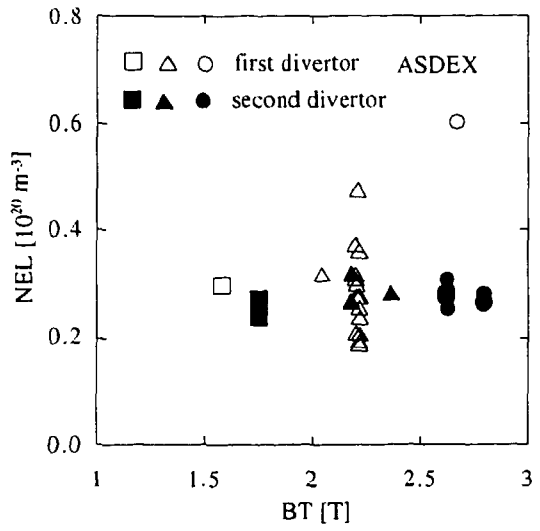

Fig.7.a

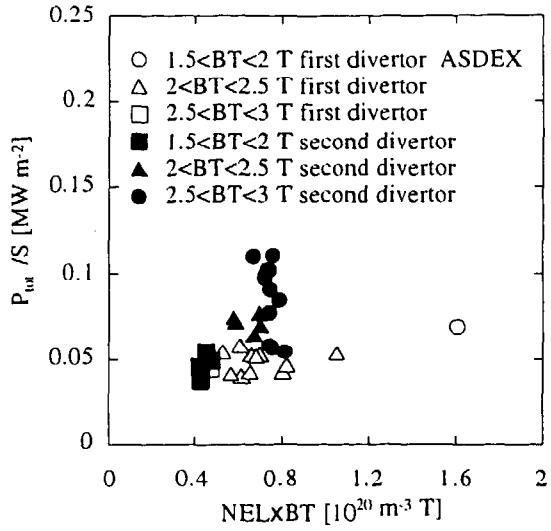

Fig.7.b

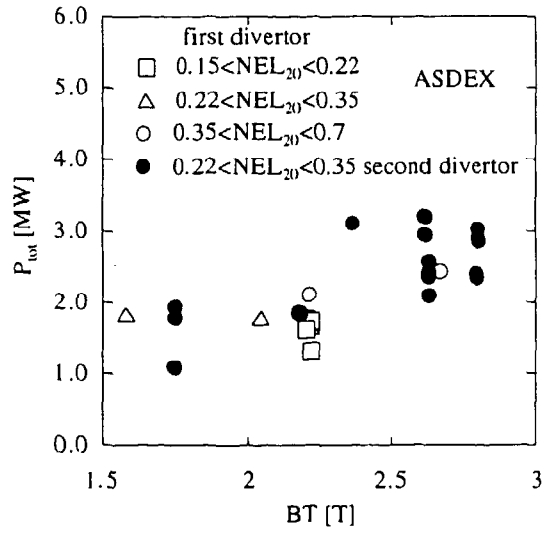

Fig.7.c

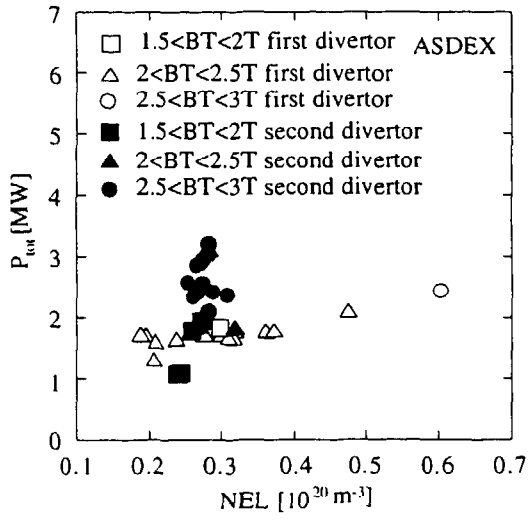

Fig.7.d

Fig.8: ASDEX Upgrade overview plots. The symbols used in a and b correspond to different BT ranges directly shown in a. The symbols used in c and d are define in the figures.

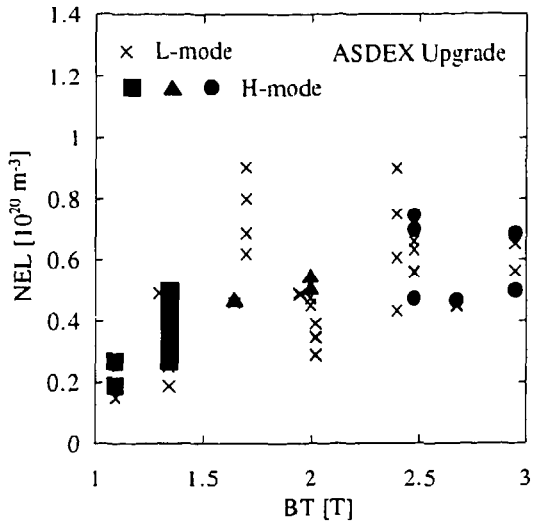

Fig.8.a

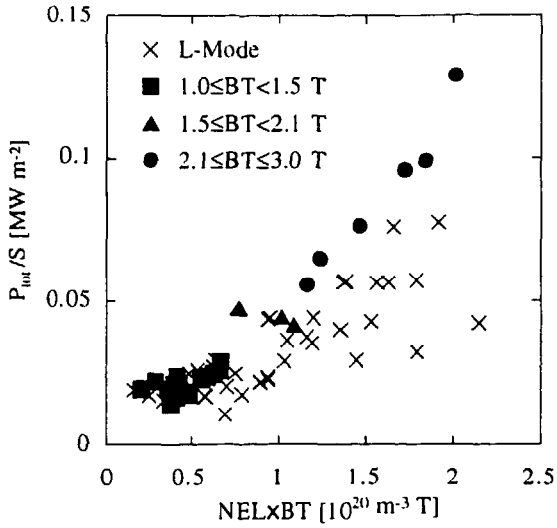

Fig.8.b

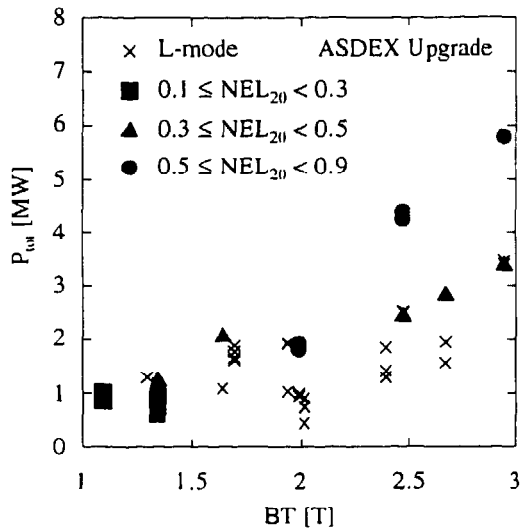

Fig.8.c

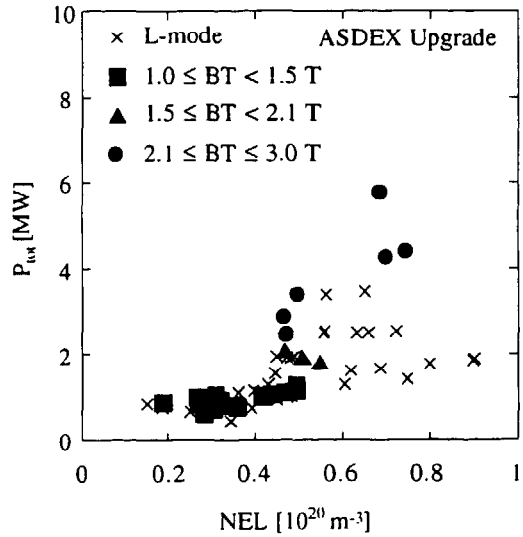

Fig.8.d

Fig.9: COMPASS-D overview plots. The symbols used in a and b correspond to different BT ranges directly shown in a. The symbols used in c and d are define in the figures.

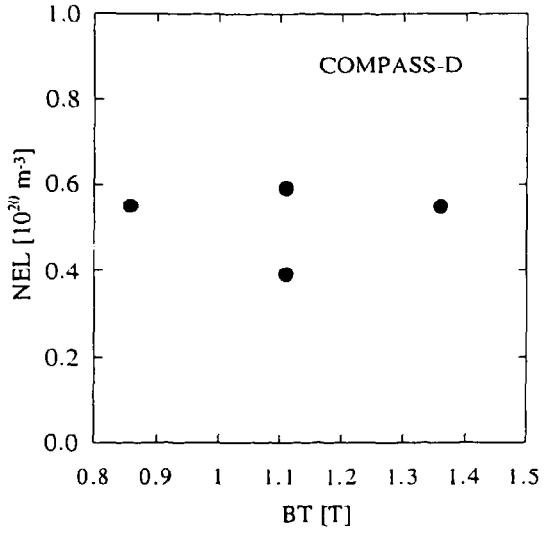

Fig.9.a

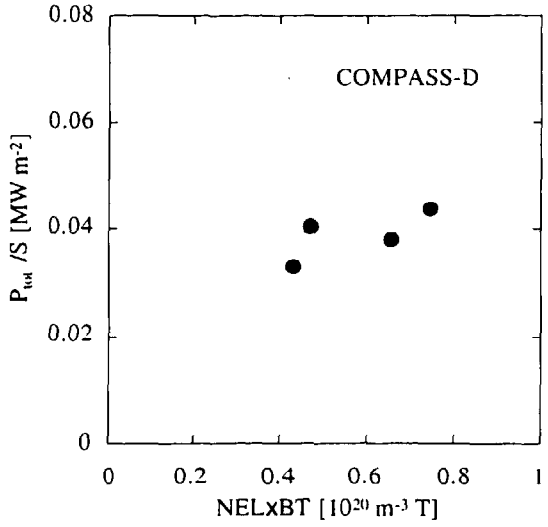

Fig.9.b

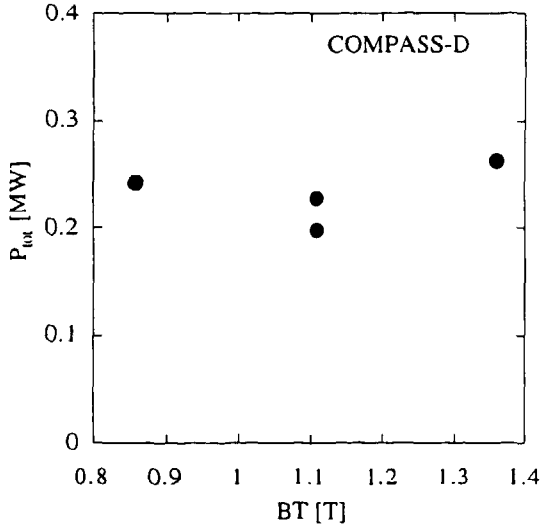

Fig.9.c

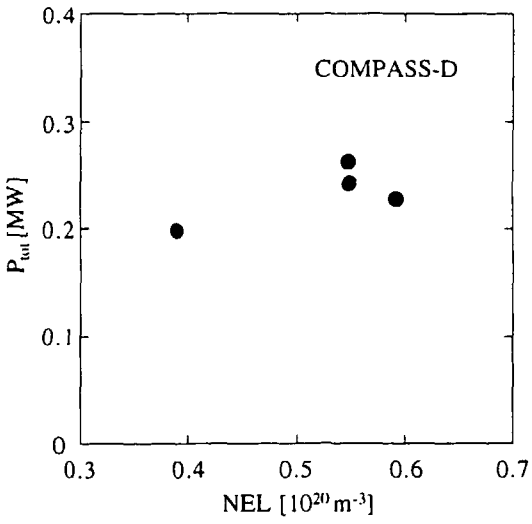

Fig.9.d

Fig.10: DIII-D overview plots. The symbols used in a and b correspond to different BT ranges directly shown in a. The symbols used in c and d are defined in the figures.

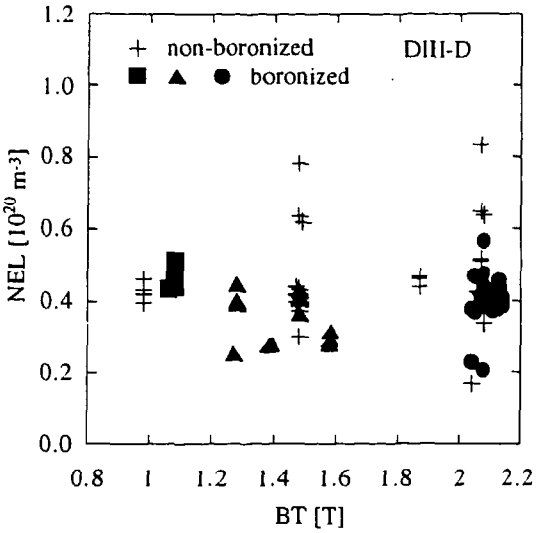

Fig.10.a

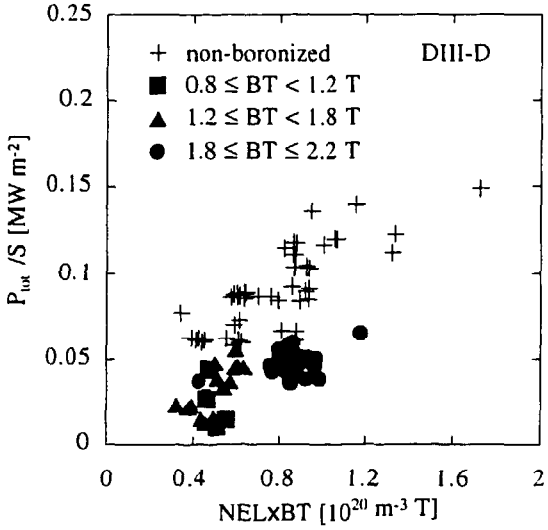

Fig.10.b

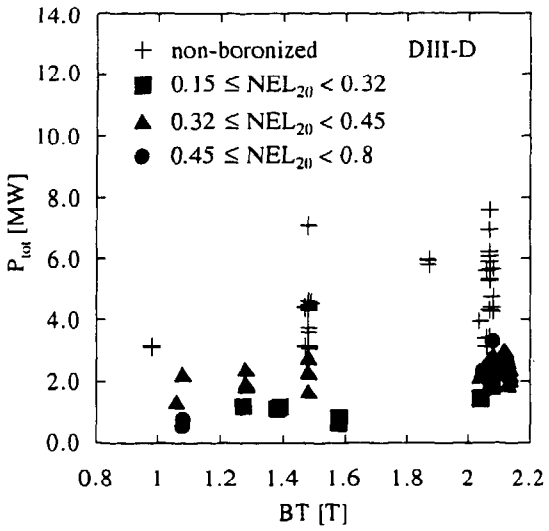

Fig.10.c

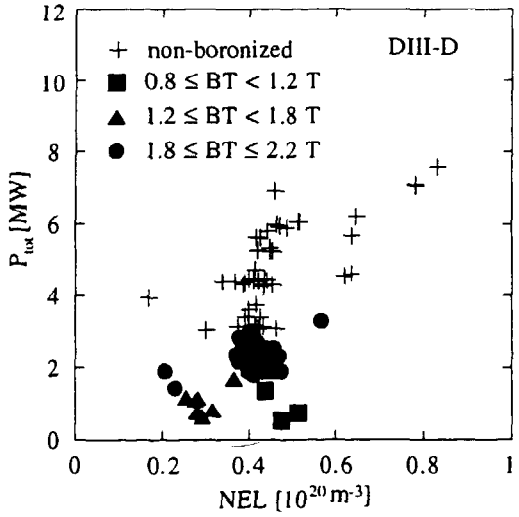

Fig.10.d

Fig.11: JET overview plots. The symbols used in a and b correspond to different BT ranges directly shown in a. The symbols used in c and d are defined in the figures.

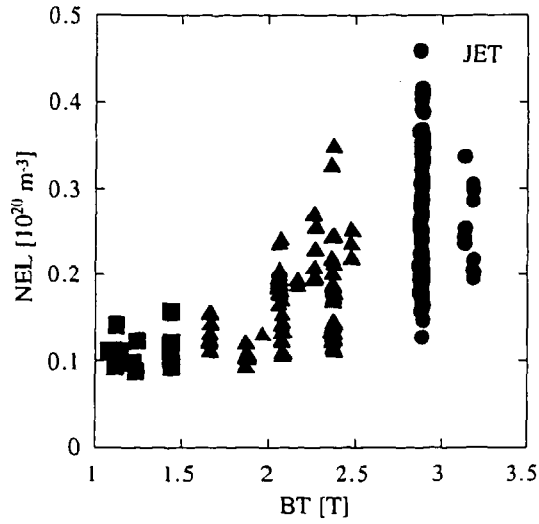

Fig.11.a

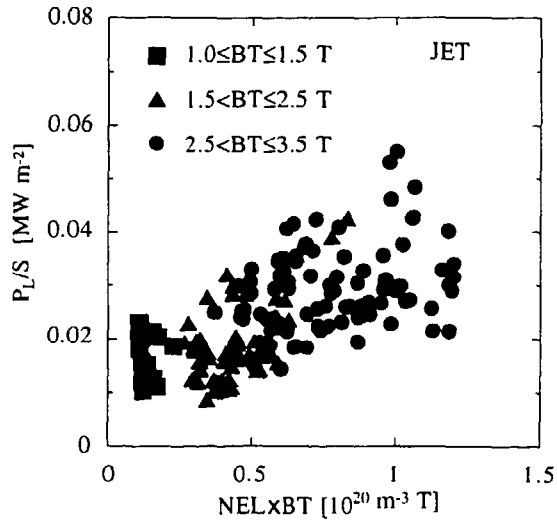

Fig.11.b

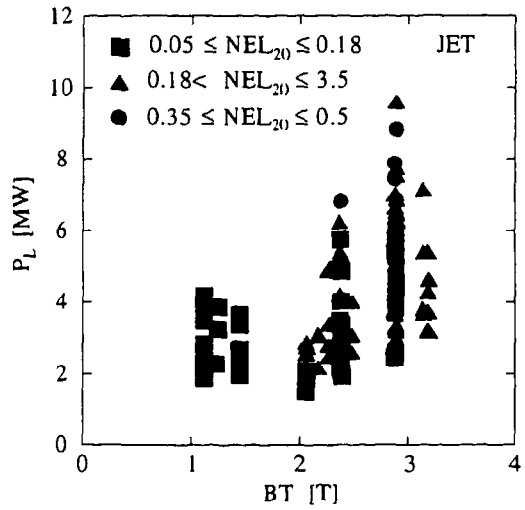

Fig.11.c

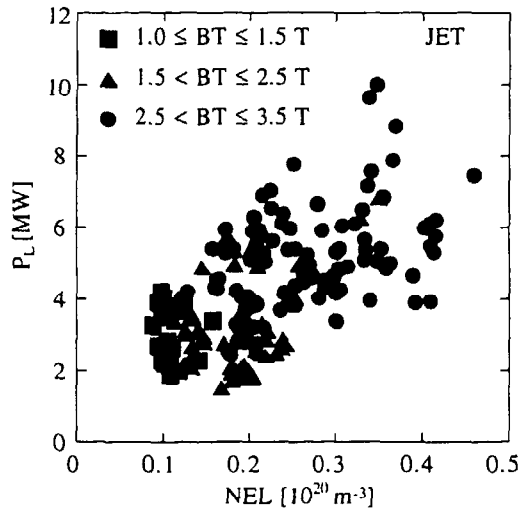

Fig.11.d

Fig.12: JFT-2M overview plots. The symbols used in a and b correspond to different BT ranges directly shown in a. The symbols used in c and d are defined in the figures.

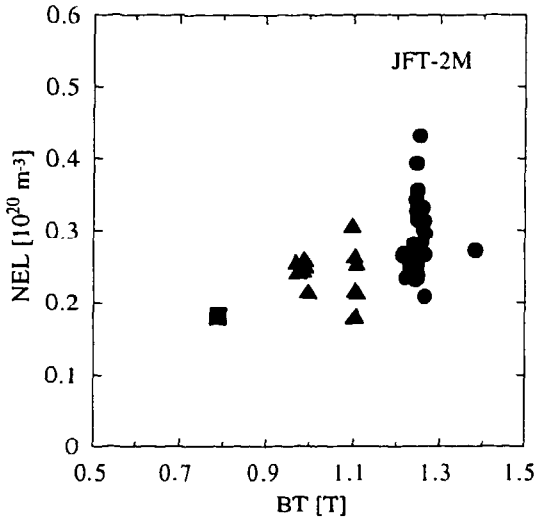

Fig.12.a

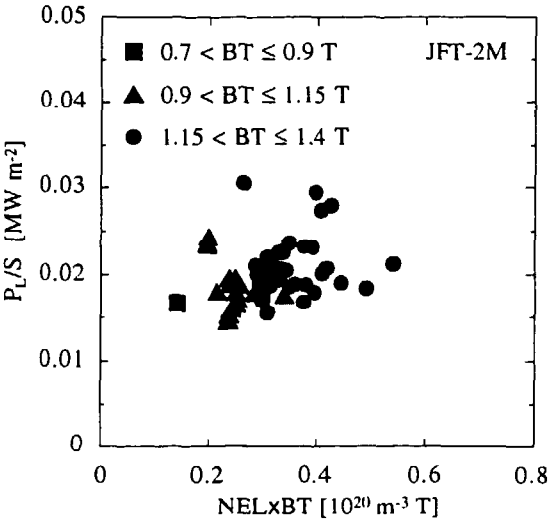

Fig.12.b

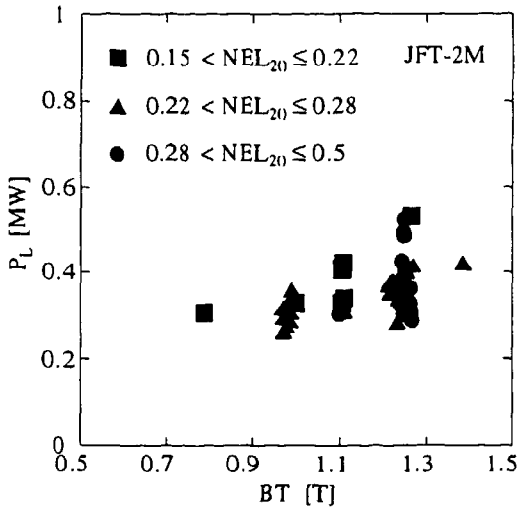

Fig.12.c

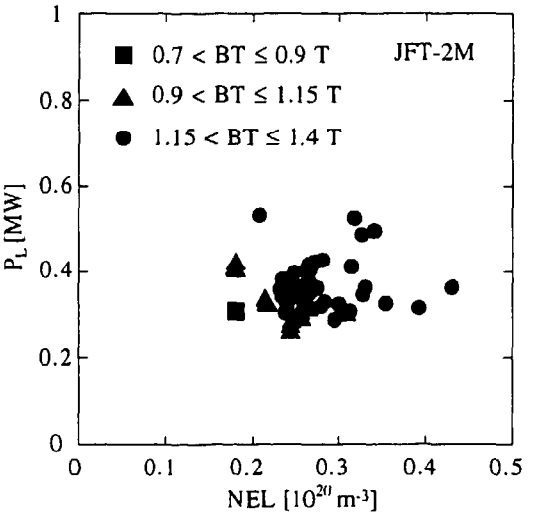

Fig.12.d

Fig.13: JT-60U overview plots. The symbols used in a and b correspond to different BT ranges directly shown in a. The symbols used in c and d are defined in the figures.

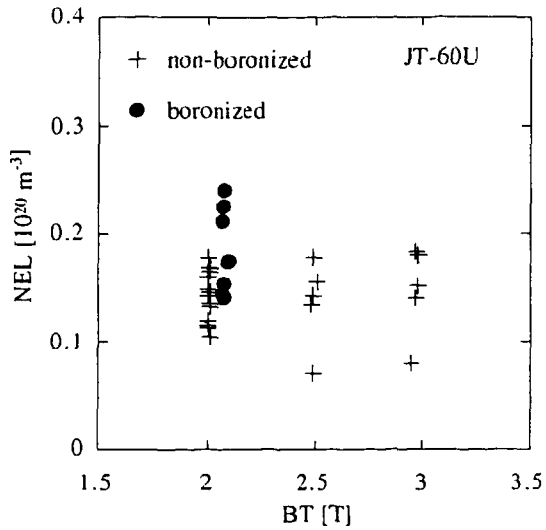

Fig.13.a

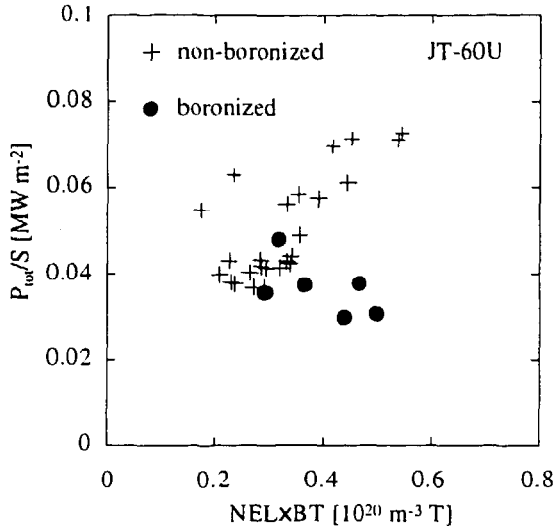

Fig.13.b

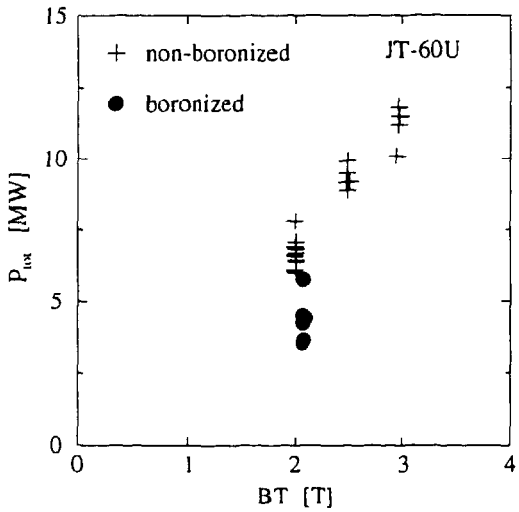

Fig.13.c

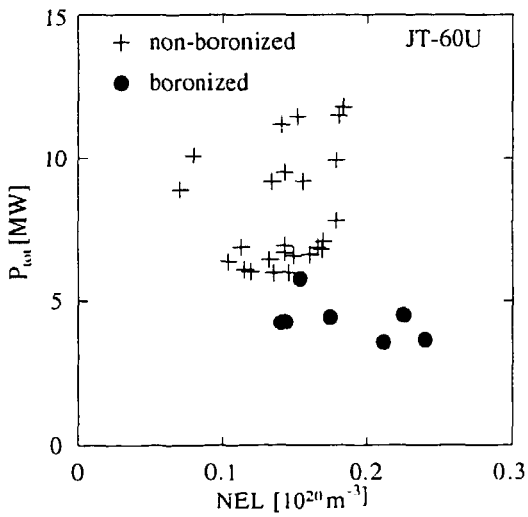

Fig.13.d

Fig.14: PBX-M overview plots. The symbols used in a and b correspond to different BT ranges directly shown in a. The symbols used in c and d are defined in the figures.

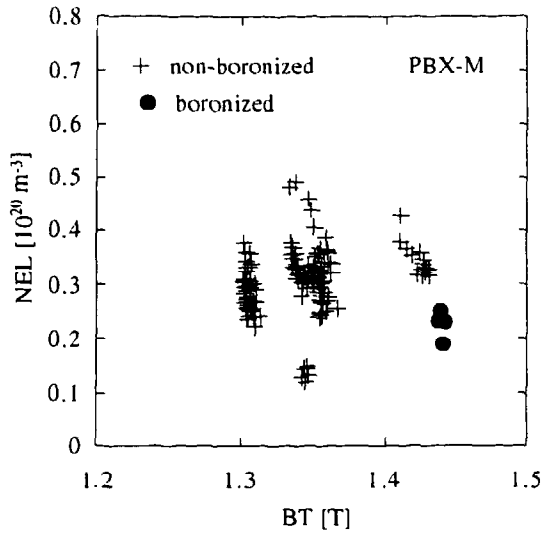

Fig.14.a

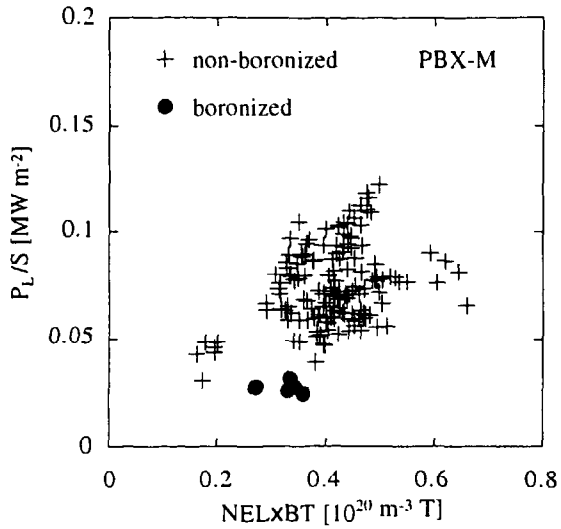

Fig.14.b

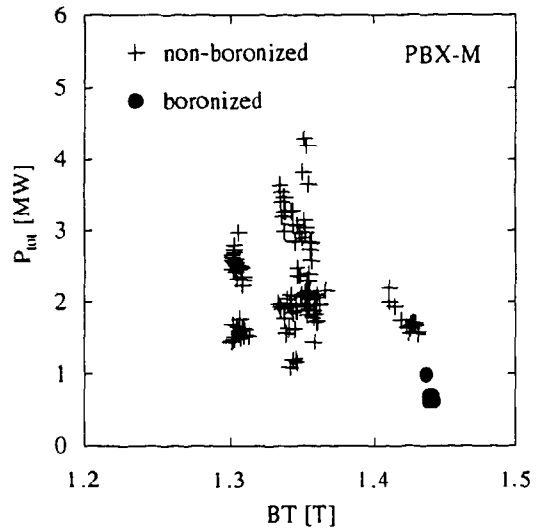

Fig.14.c

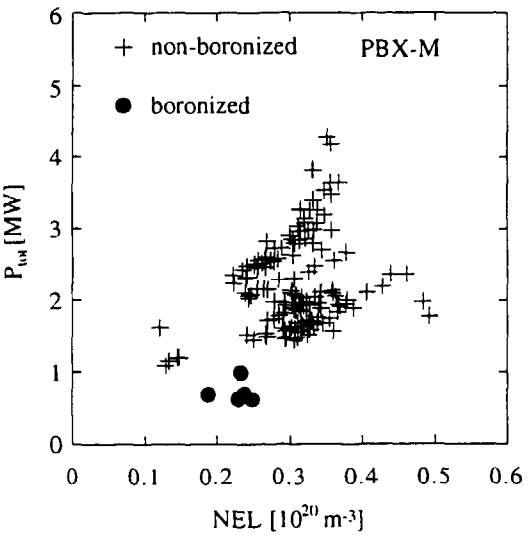

Fig.14.d

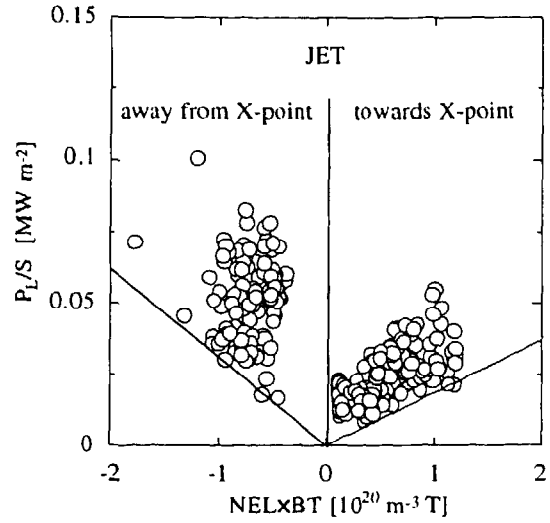

Fig.15: Influence of the ion gradB drift on threshold illustrated with JET data.

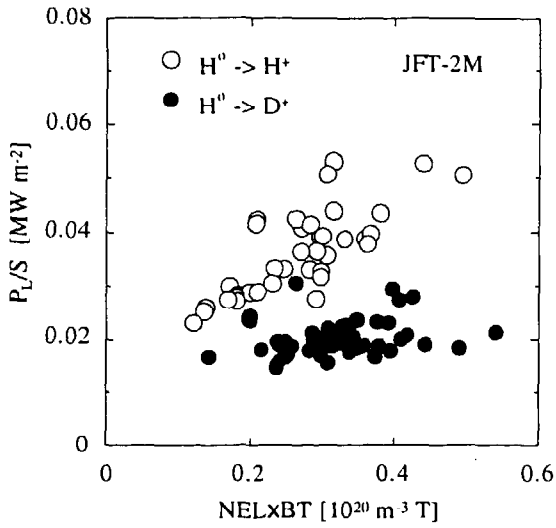

Fig.16: Influence of the isotope target plasma as illustrated with JFT-2M data.

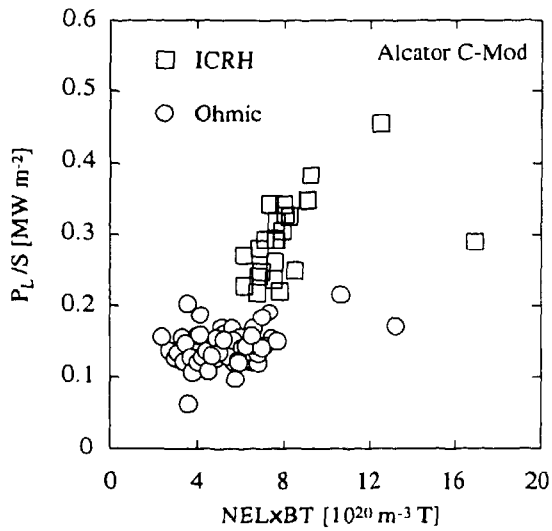

Fig.17: Comparison of the threshold with Ohmic and ICRH heating in Alcator C-Mod.

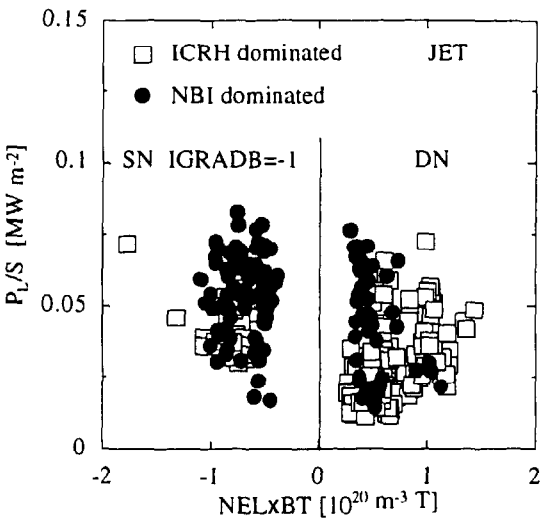

Fig.18: Comparison of the threshold in NBI and ICRH dominated discharges in JET, the criteria being P_{NBI}/P_{ICRH} larger or smaller than 1 respectively.

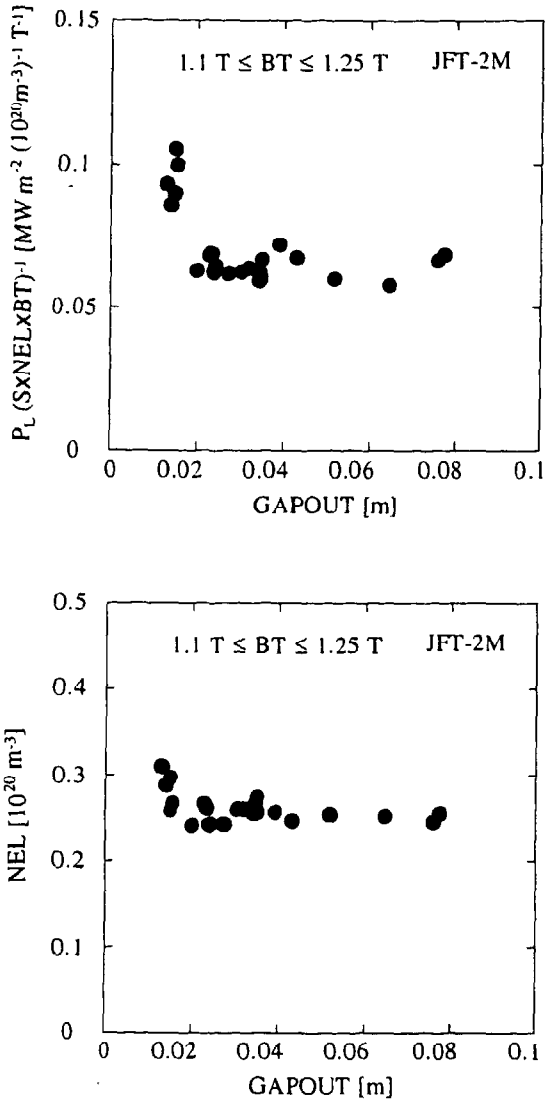

Fig.19: Effect of plasma-wall distance on threshold in JFT-2M. Top: normalized threshold versus distance between separatrix and wall. Bottom: line averaged density versus distance between separatrix and wall.

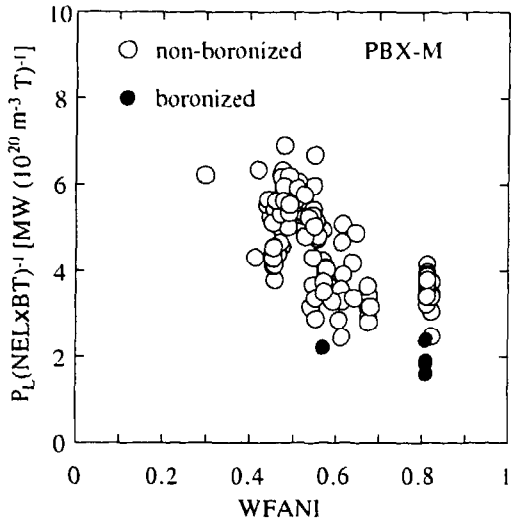

Fig.20: Influence of the fast beam ion anisotropy on threshold in PBX-M.

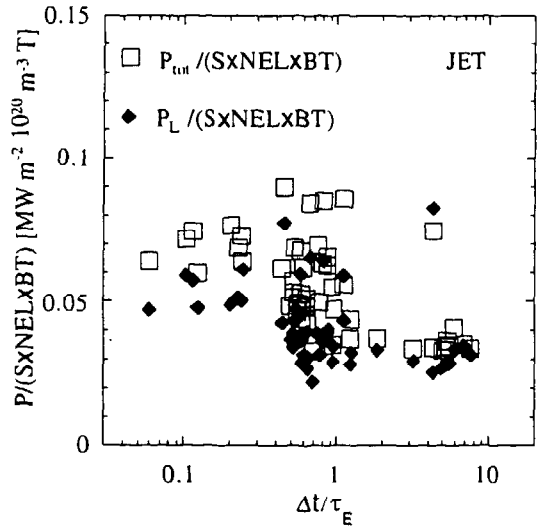

Fig.21: Variation of the normalized threshold versus time delay after the heating turn-on, normalized by the global confinement time.

Fig.22: Threshold dependence on BT for narrow density ranges in the different tokamaks. The density ranges and tokamak names are given in each plot.

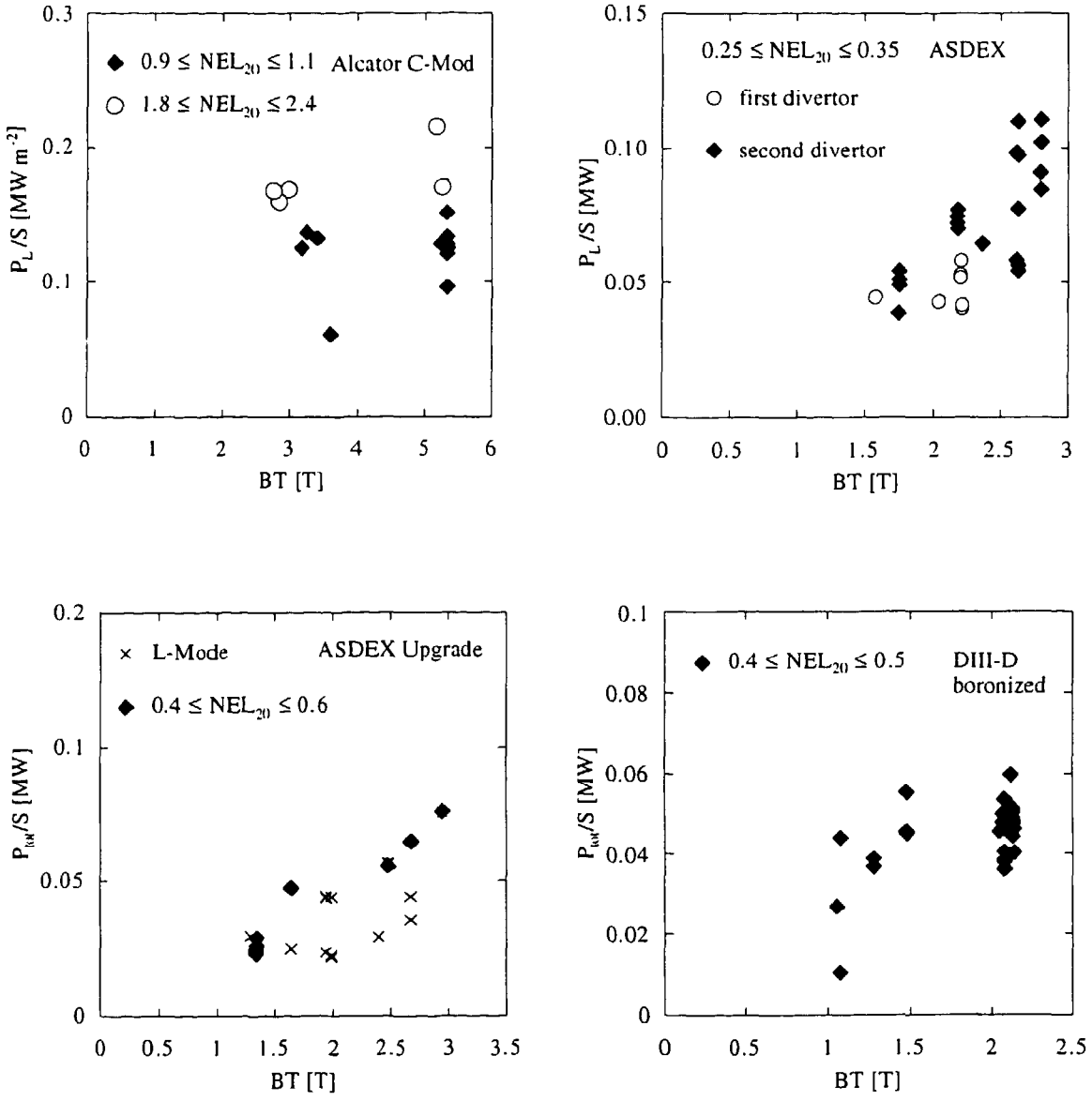

(Fig.22 continued)

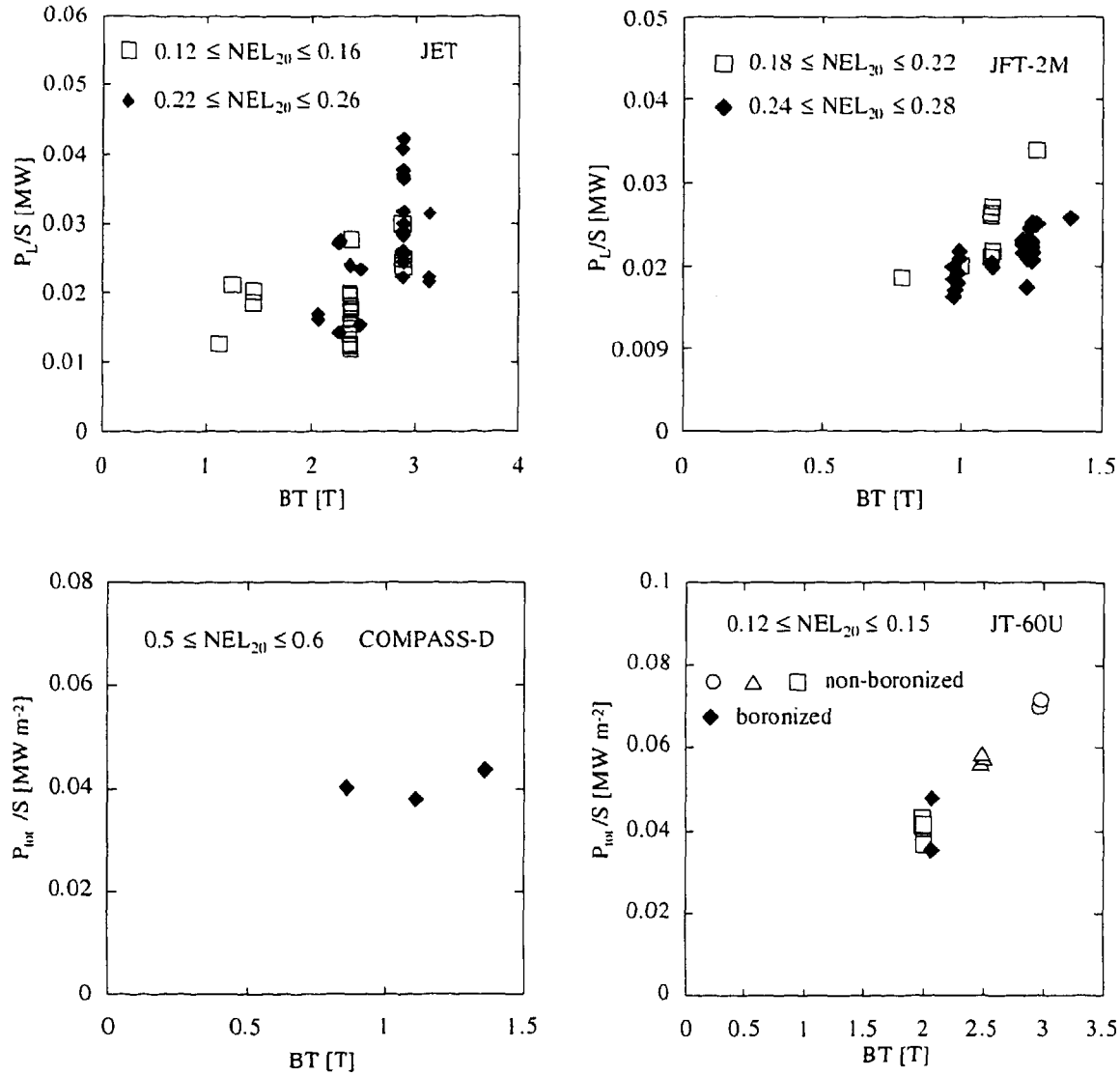

Fig.23 Threshold dependence on NEL for the different devices at fixed BT. The BT ranges and tokamak names are given in each plot.

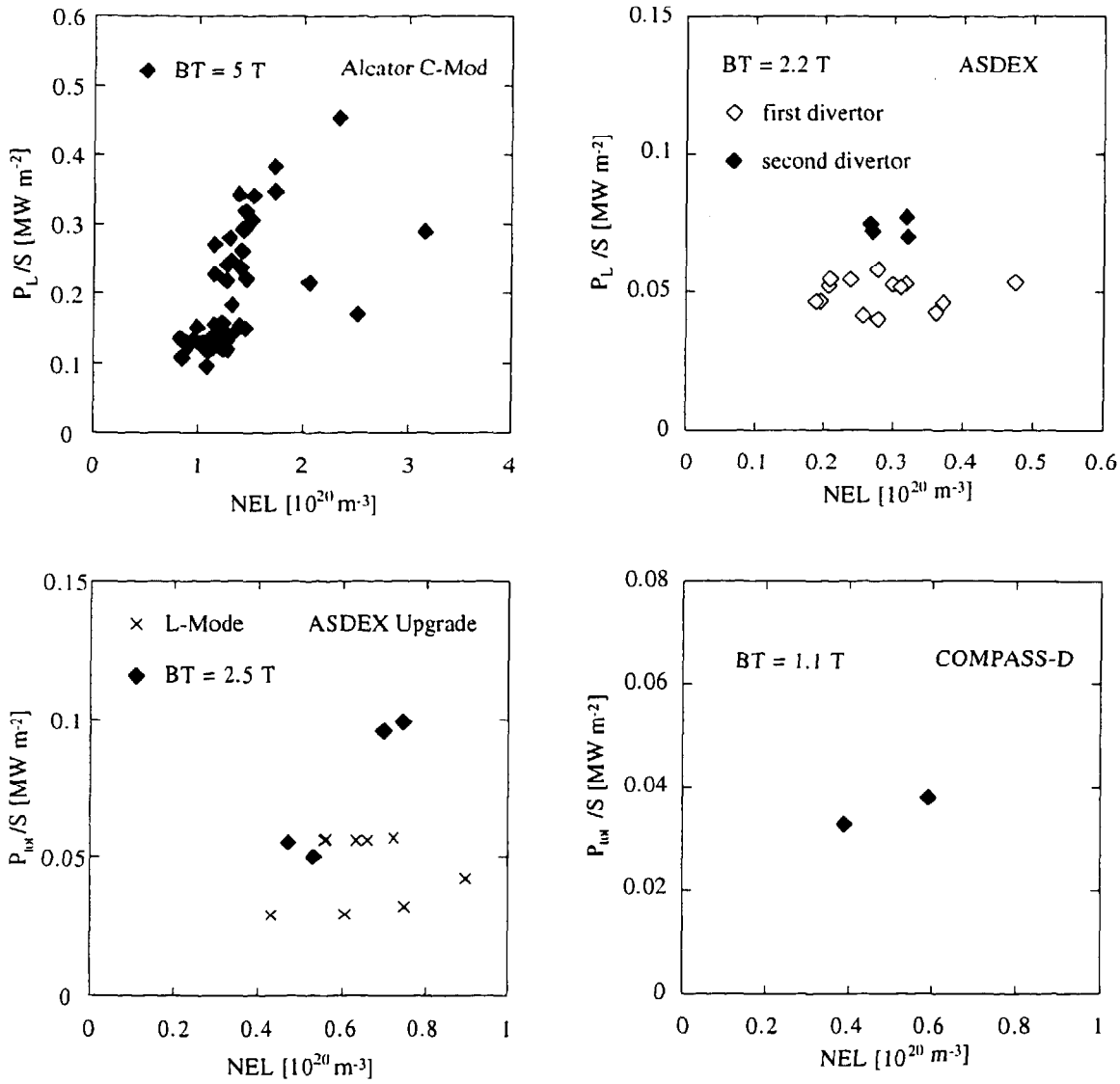

(Fig.23 continued)

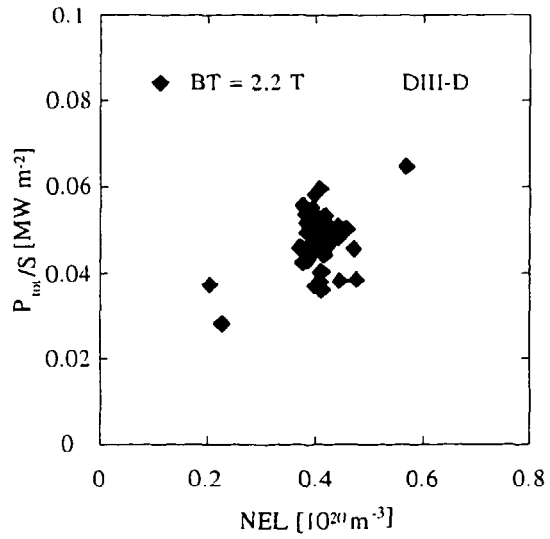

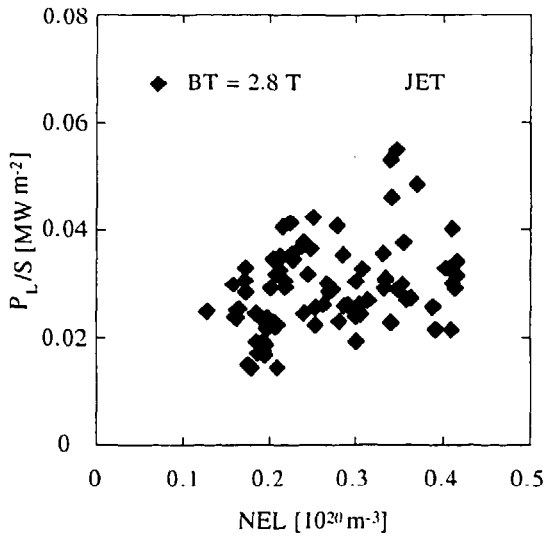

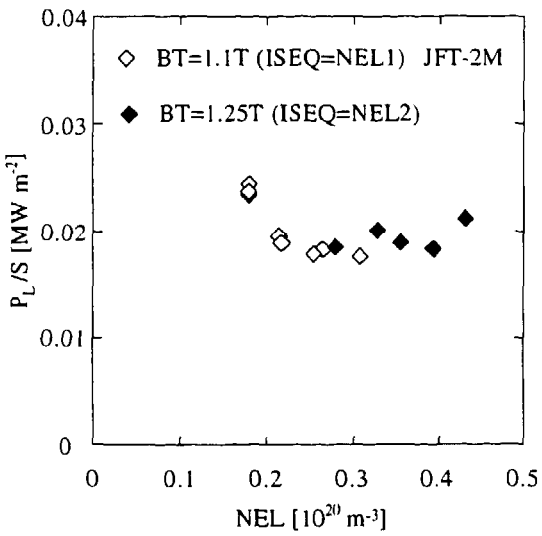

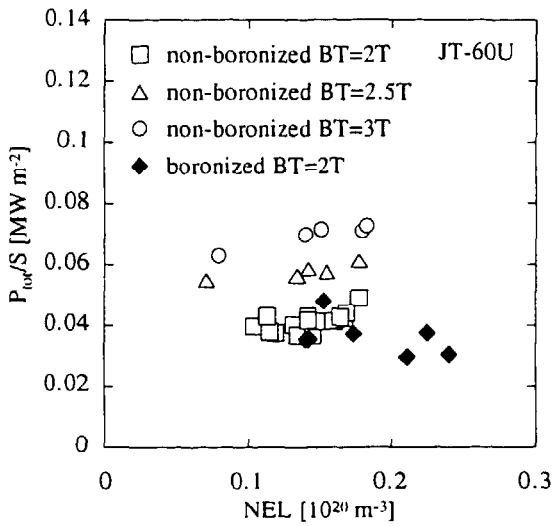

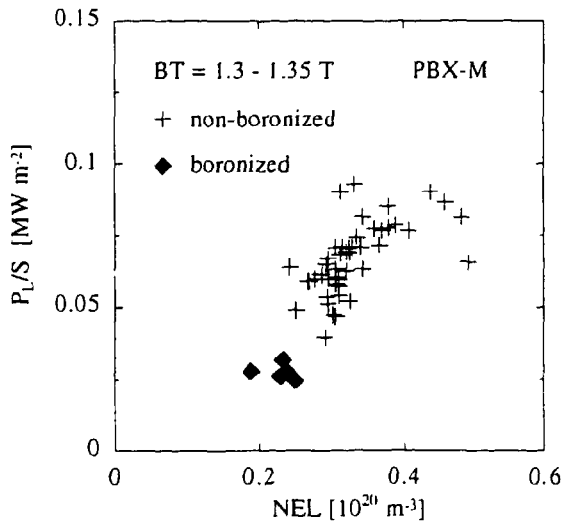

Fig.24: Results from the combined database for the four expressions derived in the text, written given in the figures and represented by the dashed lines. In these figures only boronized data from JT-60U and PBX-M were kept. For ASDEX Upgrade, COMPASS-D and DIII-D, P_{tot} is used instead of P_L, as explained in section 2 of the text.

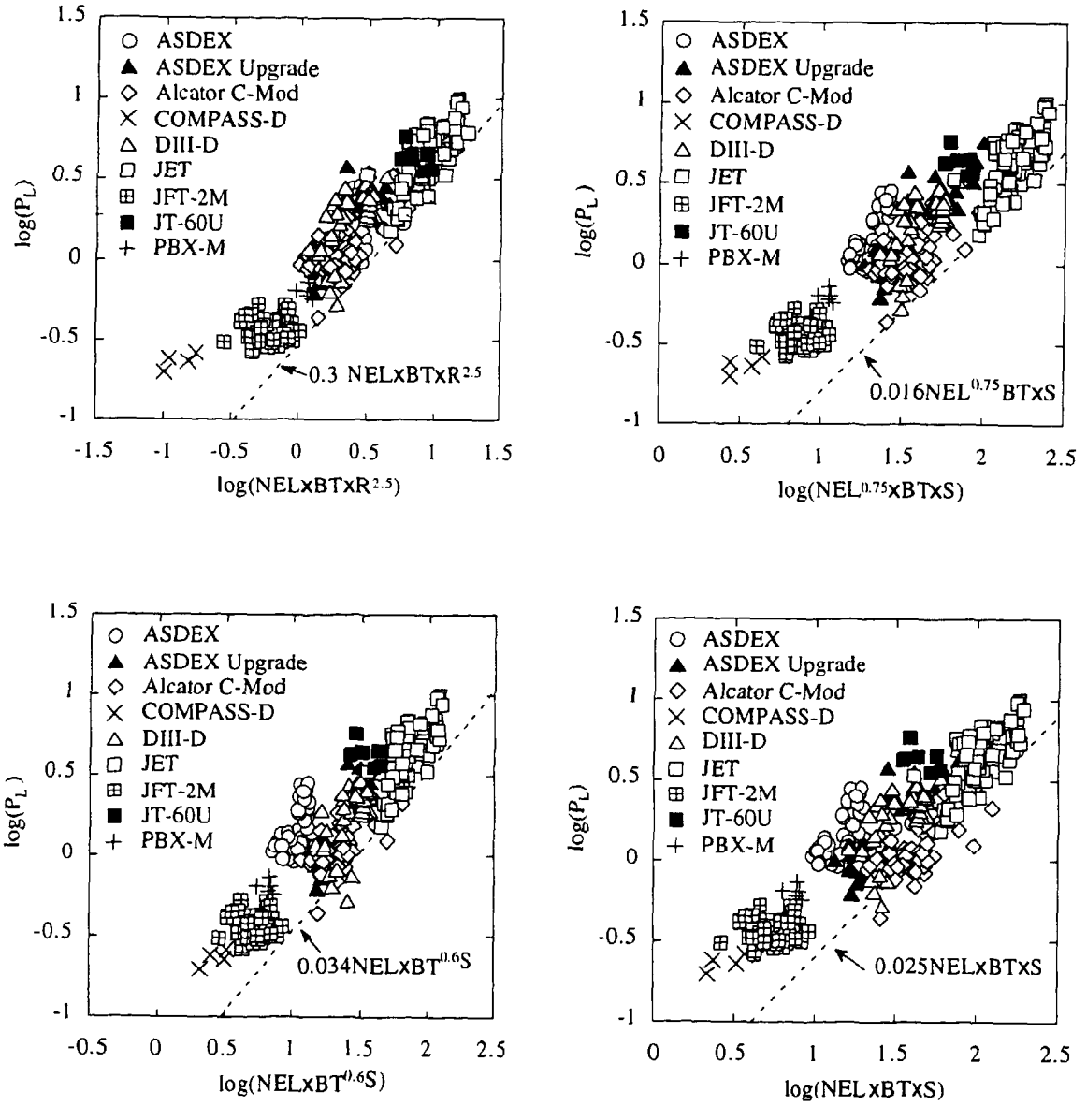

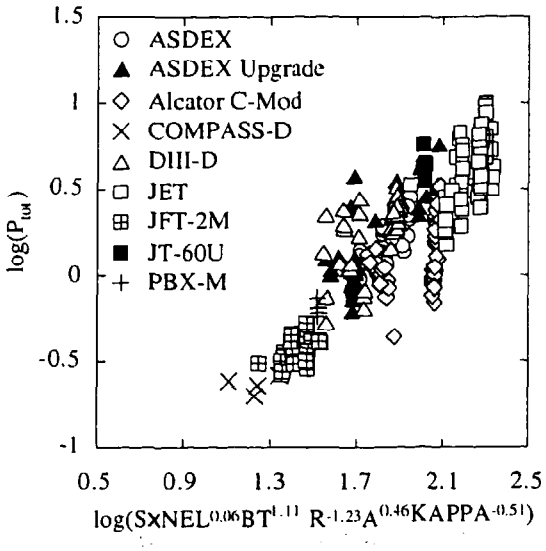

Fig.25: Result from the discriminant analysis.

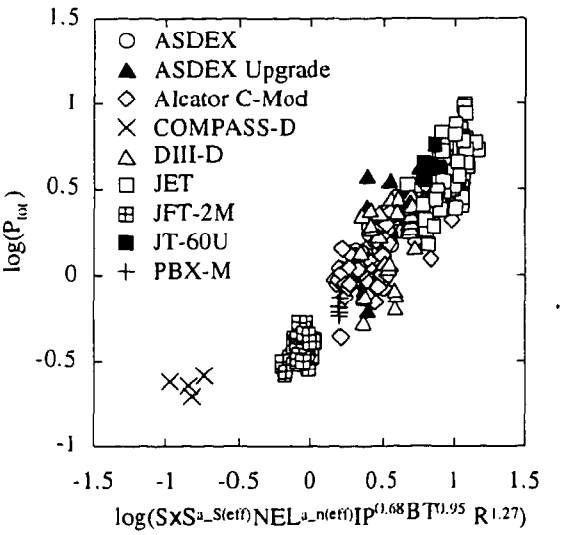

Fig.26: Result from the discriminant analysis with inter-action model, a(eff) = 1.9+0.2(lnNEL+lnS) +0.1(lnNEL)(lnS).

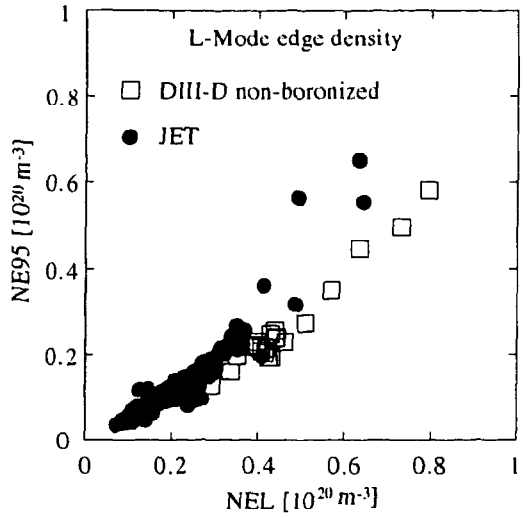

Fig.27: Edge density (NE95) versus line averaged density from DIII-D (L-Mode) and JET just before the L-to-H transition.

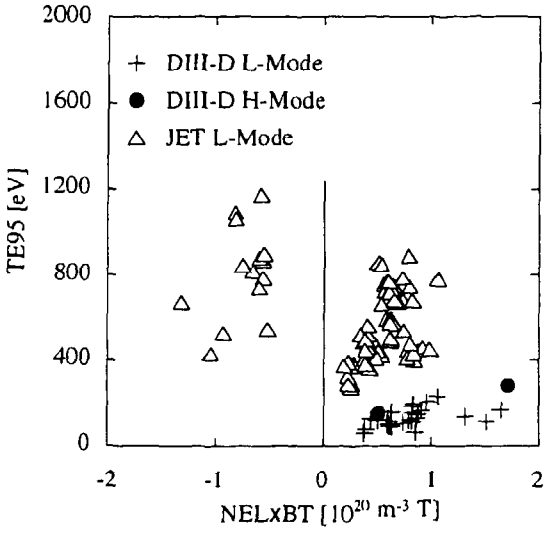

Fig.28: Edge temperature (TE95) from DIII-D (L-Mode and 2 H points) and JET just before the L-to-H transition.

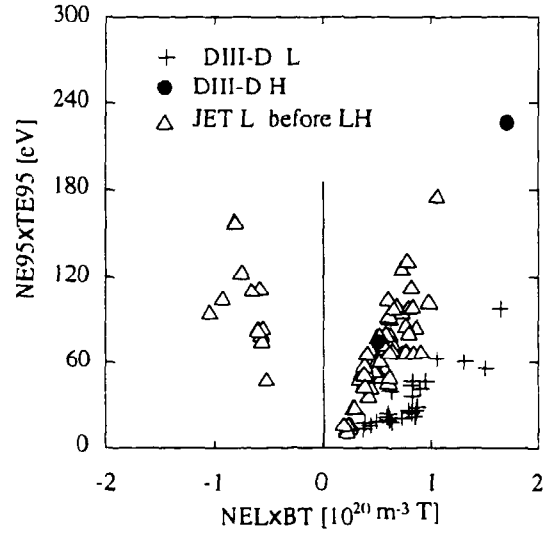

Fig.29: NE95xTE95 versus NELxBT from DIII-D (L-Mode and 2 H points) and JET just before the L-to-H transition.

Tokamak	
ASDEX	NB
ASDEX Upgrade	OHMIC, NB, IC, NBIC
DIII-D	OHMIC, NB
JET	NB, IC, NBIC, LHCD
JFT-2M	NB
JT-60U	NB
PBX-M	NB
Alcator C-Mod	OHMIC, IC
COMPASS-D	OHMIC

Table I: Heating methods in the tokamaks for discharges included in the database

Tokamak	RGEO m	AMIN m	KAPPA	SPLASMA m^2
ASDEX	1.67	0.37	1.03	24.82
ASDEX Upgrade	1.63	0.50	1.70	44.60
DIII-D	1.68	0.62	1.89	50.98
JET	2.87	1.07	1.76	173.05
JFT-2M	1.30	0.28	1.40	17.78
JT-60U	3.31	0.96	1.43	152.06
PBX-M	1.64	0.27	1.59	23.48
Alcator C-Mod	0.67	0.22	1.55	7.05
COMPASS-D	0.56	0.17	1.62	5.00

Table II: Machine geometry. The numbers given here are the mean values of the data included in the database.

TOK	|BT| [T]	NEL 20 [m^{-3}]	NEL20.|BT| [m^{-3} T]	Power [MW]
ASDEX	1.6 - 2.8	0.18 - 0.60	0.42 - 1.61	0.9 - 2.8
ASDEX Upgrade	1.0 - 3.0	0.26 - 0.74	0.29 - 2.02	0.6 - 5.7
DIII-D	1.0 - 2.2	0.20 - 0.57	0.32 - 1.18	0.5 - 3.3
JET	1.4 - 3.2	0.15 - 0.41	0.23 - 1.18	1.5 - 10.0
JFT-2M	0.8 - 1.4	0.17 - 0.43	0.14 - 0.54	0.2 - 0.5
JT60U	2.0 - 3.0	0.07 - 0.24	0.18 - 0.54	3.6 - 11.8
PBX-M	1.3 - 1.4	0.19 - 0.49	0.27 - 0.66	0.6 - 2.3
Alcator C-Mod	2.8 - 5.4	0.80 - 3.16	2.74 - 16.93	0.44 - 3.3
COMPASS-D	0.8 - 1.4	0.38 - 0.59	0.43 - 0.74	0.19 - 0.26

Table III: Parameter ranges for the diverse tokamaks of the database.

TOK	Plasma facing components	Wall coating
ASDEX	C, Stainless steel	none, boronization
ASDEX Upgrade	C, Stainless steel	boronization
DIII-D	C, inconel	none, boronization
JET	C, Be, Inconel	none, Be-evaporation
JFT-2M	C, Stainless steel	none, Ti-gettering
JT-60U	C, inconel	none, boronization
PBX-M	Stainless steel	none, boronization
Alcator C-Mod	Molybdenum	none
COMPASS-D	C	boronization

Table IV: Plasma facing components and wall coating

PHASESEL	PHASE
L	L, OHM
LA	LA, OHMA
HL	HL, HSELMOHM
HA	HA, HGELMA, HGELMHA, HSELMA
LH	LH, LHGELM, LHLHL, LHLHLA, LHSELM, OHMD, OHMH, OHMHSELM, OHMP

Table V: Assignment of the different values of the database variable PHASE to the aggregated variable PAHSESEL. As explained in the text, dithering phases were not included.

TOK	OBS L, H	RMSE	$c_{P/S}$	c_{NEL}	c_{BT}	c'	a_{NEL}	a_{BT}
ASDEX	93, 73	0.280	0.47 (0.03)	0.24 (0.09)	-0.57 (0.14)	-1.77 (0.18)	-0.52	1.21
ASDEX Upgrade	42, 26	0.363	0.78 (0.12)	-0.27 (0.19)	-0.97 (0.17)	-3.54 (0.64)	0.35	1.24
Alcator C-Mod	112, 69	0.459	0.68 (0.11)	-0.46 (0.14)	-0.95 (0.21)	-3.96 (0.65)	0.69	1.40
DIII-D_b	123, 131	0.384	0.82 (0.07)	0.22 (0.16)	-0.70 (0.15)	-2.88 (0.43)	-0.27	0.86
JET	152, 237	0.359	0.72 (0.06)	0.13 (0.06)	-0.95 (0.11)	-3.36 (0.25)	-0.18	1.32
JFT-2M	47, 127	0.436	0.31 (0.18)	0.67 (0.22)	-0.69 (0.38)	-0.59 (0.68)	-2.14	2.23
JT-60U	12, 25	0.165	1.00 (0.07)	0.05 (0.12)	-1.25 (0.24)	-4.12 (0.35)	-0.05	1.25

Table VI: Results from the discriminant analysis per tokamak. The number of observations is separated in L and H giving the number of H-mode and L-mode points taken into account respectively. COMPASS-D and PBX-M could not be included because only observations for PHASESEL= H-mode were available. From DIII-D only the boronized shots are included. Some JET points with NEL < 1.0 10^{19} m^{-3} or H-mode with P_{tot} < 3.5 MW have been omitted. Engineering units with NEL in 10^{19} m^{-3}.

OBS L,H	RMSE	$c_{P/S}$	c_{NEL}	c_{BT}	c_R	c_A	c_{KAPPA}	c'	a_{NEL}	a_{BT}	a_R	a_A	a_{KAPPA}
581,693	0.401	0.58 (0.02)	-0.04 (0.04)	-0.65 (0.04)	0.72 (0.15)	-0.27 (0.13)	0.30 (0.13)	-1.77 (0.26)	0.06	1.11	-1.23	0.46	-0.51

Table VII: Results from the discriminant analysis for the combined database including all 9 tokamaks. A = RGEO/AMIN. For DIII-D only the boronized shots were taken into account. Engineering units with NEL in 10^{19} m^{-3}.

RMSE	$c_{P/S}$	c_B	c_{IP}	c_R	c'	a_S(eff)	a_{NEL}(eff)	a_B	a_{IP}	a_R
0.380	0.61	-0.58 (0.06)	-0.41 (0.05)	-0.77 (0.21)	-0.49 (0.21)	1 - 0.2lnS	-1.84 + 0.45lnNEL + 0.17lnS	0.95	0.68	1.27

Table VIII: Results from the discriminant analysis with interaction included. Same dataset as in Table VII.

APPENDIX 1

H-MODE THRESHOLD VARIABLES

List of variables for ITERTH.DB1 H-mode threshold database

The time averaging for the majority of data is ± 2 ms for Alcator C-Mod, ± 2 ms for ASDEX, ± 10 ms for ASDEX Upgrade, ± 5 ms for DIII-D, ± 25 ms for JET, ± 2.5 ms for JFT-2M, ± 5 ms For JT-60U, ± 3.75 ms for PBX-M. The MHD analyses from Alcator C-Mod, ASDEX Upgrade and DIII-D use results from full equilibrium codes. Data from JET, PBX-M, ASDEX and JFT-2M are obtained with a current filament approach except for some of the JFT-2M variables (RMAG, q_{95}, $\beta_I + 0.5\, l_i$, β_p, B_T, W) which are calculated with a full equilibrium fit. In the variable list the abbreviation Na is used if a variable is not available and the normal level of accuracy of a variable is given as a percentage in brackets (often without further explanation).

Parameters

General

1. **TOK:** This value designates which tokamak has supplied the data. Possible values are: ASDEX, AUG, CMOD, COMPASS, D3-D, JET, JFT2M, JT60U or PBXM.

2. **UPDATE:** The date of the most recent update for any variable listed in the database. The format is YYMMDD (Year-Month-Day).

3. **DATE:** The date the shot was taken. The format is YYMMDD.

4. **SHOT:** The shot from which the data are taken.

5. **TIME:** Time during the shot at which the data are taken in seconds.

6. **AUXHEAT:** Type of auxiliary heating. Possible values are:

NONE	:	No Auxiliary heating
NB	:	Neutral Beam Injection
IC	:	Ion Cyclotron Resonance Heating
EC	:	Electron Cyclotron Resonance Heating
LH	:	Lower Hybrid Current Drive
NBIC	:	Combined NBI + ICRH
ICLH	:	Combined ICRH + LHCD
NBEC		Combined NBI + EC

7. **PHASE:** The phase of the discharge at TIME. The possible values for PHASE are divided into 4 groups:

   1) Ohmic timepoints

OHM: Ohmic
OHMH: Ohmic pre-transition to H-mode
OHMD: Ohmic pre-transition to Dithering H-mode
OHMAi (i=1,2,...):L-mode after one given H-phase, ordered by i, i= 1 being the first time slice after the corresponding HL transition

2) L-mode timepoints
L: Steady state L-mode
LAi (i=1,2,...):L-mode after one given H-phase, ordered by i, i= 1 being the first time slice after the corresponding HL transition
LD: L-mode pre-transition to Dithering H-mode
LH: L-mode pre-transition to H-mode

3) H-mode timepoints just after the L-H transition
LHLHLA: H-mode with frequent L-H transitions
DA: Dithering H-mode
HA: ELM-free H-mode
HSELMA: H-mode with small ELMs
HGELMA: H-mode with giant ELMs
HGELMHA: H-mode with high frequency giant ELMs

4) H-mode confinement timepoints
LHLHL: H-mode with frequent L-H transitions
D: Dithering H-mode
DH: ? (DIII-D to explain)
H: ELM-free H-mode
HSELM: H-mode with small ELMs
HGELM: H-mode with giant ELMs
HGELMH: H-mode with high frequency giant ELMs

8. ONTIME: The time of the start of auxiliary heating in seconds.

9. AUXTIME: The time in seconds when the last change in auxiliary power before TIME occurred.

10. LHTIME: The time of the transition from a non-H-mode phase to an H phase in seconds (non-H-mode phase generally Ohmic or L-mode). This time is:

- for non-H-mode phases, the time of the next LH transition, if data for the corresponding H phase are included in the database
- for H-mode phases, the time of the corresponding LH transition

11. ELMTIME: The time of the first ELM in seconds.

12. HLTIME: The time of the transition from an H-mode phase to a non-H-mode phase. This time is:

- for non-H-mode phases, the time of the previous HL transition, if data for the corresponding H phase are included in the database
- for H-mode phases, the time of the next HL transition, if data for the corresponding transition are included in the database.

13. OFFTIME: The time of the end of auxiliary heating in seconds.

14. CAUSE: Identifier of the cause of an LH or HL transition. The possible values are:

SWTTH when LH triggered by a sawtooth
GASOFF when LH triggered by gas puffing turn-off
GASON when H-mode (possibly) prevented or HL triggered by gas puffing.
RAD when H-mode (possibly) prevented or HL triggered by high radiation losses.
DENS when H-mode (possibly) prevented or HL triggered by high density.
ELM: HL transition caused by an ELM.
UNKNOWN when the H-mode is obviously prevented or HL triggered by an unknown phenomenon.

15. TRTIME: Duration of the transition in seconds. This is taken to be the duration of the drop in the D_α emission.

16. ISEQ: Parameter scan identifier

Possible options for ASDEX are:

ISEQ	Explanation
NONE	No particular scan
P1	
BT2P4	
BT3	
BT4	
BT5	
BT6	
BT7	

Possible options for ASDEX Upgrade are:

ISEQ	Explanation
NEi ($1 \leq i \leq 3$)	

BTi (1≤ i ≤4)	

Possible options for DIII-D are:

ISEQ	Explanation
B1N1P01X1	
N1P02	
N1P03	
B1P04	
B1P05	
P06X1	
B2I1P07	
I1P08	
P09	
P10	
N1P11	
B2P12	
P13	
N2P14	
P15X1	
P16X1	
P17X1	
P18X1	
P19	

Possible options for JFT-2M are:

ISEQ	Explanation
IPBT1	
IPBT2	
XPHE1	
XPHE2	
DN1	
ENBI1	
ENBI2	
ENBI3	

ENBI4	
GO1IP1BT1	
GO1IP1BT2	
GO1IP1BT3	
GO1IP2BT3	
GO1IP3BT3	
AMINIP1	
NOEVAP1	
NOEVAP2	
XPLIM1	
IGB1IP1M1	
IGB1IP2M1	
IGB1IP3M1	
IGB1IP4M1	
IGB1IP5M1	
IGB1IP1M2	
IGB1IP2M2	
IGB1IP3M2	
IGB1IP4M2	
IGB1IP5M2	
NEL1	
NEL2	

17. **TPI:** Time point indicator (ASDEX only). Possible values are:
1 - 3 : Ohmic points
4 - : L- or H- mode points

Plasma Composition

18. **PGASA:** Mass number of the plasma working gas. Possible values are:
1 (Hydrogen), 2 Deuterium), 3 (^3He) or 4 (^3He).

19. **PGASZ:** Charge number of the plasma working gas. Possible values are:
1 (Hydrogen or Deuterium) or 2 (Helium).

20. **BGASA:** Mass number of the neutral beam gas. Possible values are:
1 (Hydrogen), 2 (Deuterium), 3 (^3He) or 4 (^4He).

21. **BGASZ:** Charge number of the neutral beam gas. Possible values are:
1 (Hydrogen or Deuterium) or 2 (Helium).

22. **BGASA2:** Mass number of the second neutral beam gas (JET only). Possible values are: 1 (Hydrogen), 2 (Deuterium), 3 (^3H_e) or 4 (^4H_e).

23. **BGASZ2:** Charge number of the second neutral beam gas (JET only). Possible values are: 1 (Hydrogen or Deuterium) or 2 (Helium).

24. **BGASA3:** Mass number of Tritium PINI's (JET only). Possible values are: 2 (Deuterium with 1% Tritium) or 3 (Tritium).

25. **BGASZ3:** Charge number of Tritium PINI's (JET only). Possible value is: 1 (Deuterium with 1% Tritium or 100% Tritium).

26. **MEFF:** Effective atomic mass in AMU.
= PGASA if PINJ = 0.
= 0.5 (PGASA + A_{BEAM}) if PINJ > 0, where A_{BEAM} is the appropriate average of BGASA, BGASA2 and BGASA3.

Geometry

27. **RGEO:** The plasma geometrical major radius in metres, from an MHD equilibrium fit, defined as the average of the minimum and the maximum radial extent of the plasma.
Normal level of accuracy is Alcator C-Mod (0.6%), ASDEX (0.5%), ASDEX Upgrade (0.5%), DIII-D (0.6%) JET (1%), JFT-2M (0.75%), JT-60U (0.5%), PBX-M (0.65%).

28. **RMAG:** The major radius of the magnetic axis in metres from an MHD equilibrium fit.
Normal level of accuracy is Alcator C-Mod (1%), ASDEX (0.5%), ASDEX Upgrade (1%), DIII-D (1%), JET (2%), JFT-2M (2%), JT-60U (0.5%), PBX-M (1%).

29. **ZMAG:** Vertical position of the magnetic axis in metres from an MHD equilibrium fit.
Normal level of accuracy is Alcator C-Mod (1%), ASDEX (0.5%), ASDEX Upgrade (0.5%), DIII-D (1%), JET (2%), JFT-2M (2%), JT-60U (0.5%), PBX-M (1%).

30. **R95:** The radius of the near 95% flux surface in metres determined from the magnetic equilibrium fit.
Normal level of accuracy is Alcator C-Mod (0.5 cm), ASDEX (1 cm), ASDEX Upgrade (1 cm), DIII-D (0.5 cm), JET (2 cm), JFT-2M (Na), JT-60U (Na), PBX-M (Na).

31. **AMIN:** The horizontal plasma minor radius in metres from a MHD equilibrium fit.
Normal level of accuracy is Alcator C-Mod (0.5%), ASDEX (1%), ASDEX Upgrade (1%), DIII-D (0.5%), JET (3%), JFT-2M (3%), JT-60U (1%), PBX-M (3%).

32. **GAPIN:** The distance between the dominant separatrix flux surface and the inside wall at the mid plane in metres from an MHD equilibrium fit. Normal level of accuracy is Alcator C-Mod (0.5 cm), ASDEX (1 cm), ASDEX Upgrade (1 cm), DIII-D (0.5 cm), JET (2 cm), JFT-2M (Na), JT-60U (1 cm), PBX-M (Na).

33. **GAPOUT:** The distance between the dominant separatrix flux surface and the outside wall at the mid plane in metres for an MHD equilibrium fit. Normal level of accuracy is Alcator C-Mod (0.5 cm), ASDEX (1 cm), ASDEX Upgrade (1 cm), DIII-D (0.5 cm), JET (2 cm), JFT-2M (Na), JT-60U (1 cm), PBX-M (Na).

34. **GAPTOP:** The distance between the dominant separatrix flux surface and the top of the vessel in metres.
Normal level of accuracy is Alcator C-Mod (3 cm), ASDEX (1 cm), ASDEX Upgrade (Na), DIII-D (3 cm), JET (2 cm), JFT-2M (Na), JT-60U (1 cm), PBX-M (Na).

35. **GAPBOT:** The distance between the dominant separatrix flux surface and the bottom of the vessel in metres.
Normal level of accuracy is Alcator C-Mod (3 cm), ASDEX (1 cm), ASDEX Upgrade (Na), DIII-D (3 cm), JET (2 cm), JFT-2M (Na), JT-60U (1 cm), PBX-M (Na).

36. **SEPLIM:** The minimum distance between the dominant separatrix flux surface and either the vessel wall or limiters in metres from an MHD equilibrium fit.
Normal level of accuracy is Alcator C-Mod (0.5 cm), ASDEX (1 cm), ASDEX Upgrade (Na), DIII-D (0.5 cm), JET (2 cm), JFT-2M (1 cm), JT-60U (1 cm), PBX-M (0.5 cm).

37. **XPLIMT:** The minimum distance between the top X-point and either the vessel walls or limiters in metres from an MHD equilibrium fit. Positive XPLIMT means that the X-point is inside the vessel.
Normal level of accuracy is Alcator C-Mod (3 cm), ASDEX (Na), ASDEX Upgrade (Na), DIII-D (3 cm), JET (2 cm), JFT-2M (3 cm), JT-60U (Na), PBX-M (5 cm).

38. **XPLIMB:** The minimum distance between the bottom X-point and either the vessel walls or limiters in metres from an MHD equilibrium fit. Positive XPLIMB means that the X-point is inside the vessel.
Normal level of accuracy is Alcator C-Mod (3 cm), ASDEX (Na), ASDEX Upgrade (Na), DIII-D (3 cm), JET (2 cm), JFT-2M (3 cm), JT-60U (1 cm), PBX-M (5 cm).

39. **DRSEP:** The distance at the outer mid plane (low field side) between the dominant separatrix flux surface and the secondary x-point flux surface in meters from an MHD equilibrium fit.
Normal level of accuracy is Alcator C-Mod (0.5 cm), ASDEX (NA), ASDEX Upgrade (Na), DIII-D (0.5 cm), JET (0.2 cm), JFT-2M (Na), JT-60U (Na), PBX-M (Na).

40. **THXPT:** Poloidal angle of upper x-point (in degrees measured counter-clockwise from the outer major radius axis) with respect to the magnetic axis.
Normal level of accuracy is Alcator C-Mod (1 degree), ASDEX (3 degrees), ASDEX Upgrade (Na), DIII-D (1 degree), JET (1 degree), JFT-2M (Na), JT-60U (Na), PBX-M (Na).

41. **THXPB:** Poloidal angle of lower x-point (in degrees measured counter-clockwise from the outer major radius axis) with respect to the magnetic axis. Normal level of accuracy is Alcator C-Mod (1 degree), ASDEX (3 degrees), ASDEX Upgrade (Na), DIII-D (1 degree), JET (1 degree), JFT-2M (Na), JT-60U (Na), PBX-M (Na).

42. **KAPPA:** The plasma elongation determined from an MHD equilibrium fit. Normal level of accuracy is Alcator C-Mod (1%), ASDEX (1%), ASDEX Upgrade (1%), DIII-D (1%), JET (5%), JFT-2M (10%), JT-60U (2%), PBX-M (10%).

43. **DELTA:** The triangularity of the plasma boundary from an MHD equilibrium fit.

JET: DELTA = v + 3/(16v) $\left(\sqrt{1+32v^2}-1\right)$, where v = R2/AMIN

with R2 from the Lao-Hirshman representation of the plasma boundary.
Normal level of accuracy is Alcator C-Mod (10%), ASDEX (Na), ASDEX Upgrade (10%), DIII-D (10%), JET (10%), JFT-2M (10%), JT-60U (5%), PBX-M (25%).

44. **INDENT:** Indentation of the plasma determined from and MHD equilibrium fit.
Normal level of accuracy is only available for PBX-M (15%).

45. **AREA:** Area of plasma cross section in m^2 determined from an MHD equilibrium fit.
Normal level of accuracy is Alcator C-Mod (3%), ASDEX (3%), ASDEX Upgrade (3%), DIII-D (3%), JET (6%), JFT-2M (5%), JT-60U (2%), PBX-M (10%).

46. **SPLASMA** Plasma surface area in m^2.
For ASDEX from the formula:
For AUG the separatrix surface area from an equilibrium code.

47. **VOL:** The plasmas volume in m^3 determined from an MHD equilibrium fit.
Normal level of accuracy is Alcator C-Mod (3%), ASDEX (3%), ASDEX Upgrade (3%), DIII-D (3%), JET (6%), JFT-2M (5%), JT-60U (2%), PBX-M (10%).

48. **CONFIG:** The plasma configuration. Possible values are: SN for single null or DN for double null.
Alcator C-Mod: SNB used for singe null at the bottom of the machine.

ASDEX: DN if vertical shift ΔZ is less than 5 mm, otherwise SN.
ASDEX Upgrade: SN used for singe null at the bottom of the machine.
DIII-D: Only SN.
JET: Determined by operation session leader. SN(T) and SN (B) used for single null at the top and bottom of the machine, respectively.
JFT-2M: DN if two nulls are inside the limiter.
JT-60U: Only SN
PBX-M: Only DN

49. IGRADB: Indicates when CONFIG = SN whether the ion ∇B-drift is towards (1) or pointing away from (-1) the X-point. For CONFIG=DN IGRADB = 0.

50. XTRGT: Flag to indicate whether the x-point target is continuous or discrete toroidally. ("C" or "D").

Machine Condition

51. WALMAT: The material of the vessel wall with possible values SS for stainless steel, CSS for carbon and stainless steel, IN for Inconel, C for carbon, MO for molybdenum, and IN/C for Inconel with carbon.

52. DIVMAT: The material of the divertor tiles with possible values SS for stainless steel, C or CC for carbon, TI1 or TI2 for titanium, BE for beryllium, MO for Molybdenum, C/BE for carbon at the top and beryllium at the bottom.

53. LIMMAT: The material of the limiters with possible values BE for beryllium, C for carbon, MO for molybdenum, C/BE for carbon and beryllium.

54. EVAP The evaporated material used to cover the inside of the vessel with possible values BE for beryllium, BOROA, BOROB and BOROC for boron, TI for titanium LI for lithium and NONE for no evaporation.

Magnetics

55. BT The vacuum toroidal magnetic field in Tesla at RGEO determined from the TF coil current. Negative values for JET indicate operation with reversed toroidal field.
Normal level of accuracy is 1% for all machines.

56. IEML: Ergodic magnetic field coil current in amperes (JFT-2M only). Normal level of accuracy is JFT-2M (1%). ASDEX, DIII-D, JET, PBX-M: Na.

57. **IP:** The plasma current in amperes determined from an external Rogowski loop with vessel current subtraction. Normally negative values for JET. Positive values for JET indicate operation with reversed current.
Normal level of accuracy is Alcator C-Mod (2%), ASDEX (2%), ASDEX Upgrade (1%), DIII-D (1%), JET (1%), JFT-2M (1%), JT-60U (0.5%), PBX-M (1%).

58. **VSURF:** The loop voltage at the plasma boundary in volts.
Normal level of accuracy is Alcator C-Mod (Na), ASDEX (5%), ASDEX Upgrade (10%), DIII-D (Na), JET (5%), JFT-2M (5%), JT-60U (20%), PBX-M (50%).

59. **Q95:** The plasma safety factor from the MHD equilibrium fit evaluated at the flux surface that encloses 95% of the total poloidal flux.
Normal level of accuracy is Alcator C-Mod (3%), ASDEX (15%), ASDEX Upgrade (5%), DIII-D (3%), JET (10%), JFT-2M (10%), JT-60U (5%), PBX-M (10%).

60. **BEILI2:** This quantity is determined from MHD and represents $\beta_i + 0.5\ l_i$, where β_i is the Shafranov beta and l_i the internal inductance.
Normal level of accuracy is Alcator C-Mod (3%), ASDEX (10%), ASDEX Upgrade (3%), DIII-D (3%), JET (5%), JFT-2M (10%), JT-60U (5%), PBX-M (10%).

61. **BEIMHD:** Beta Shafranov from MHD.
Normal level of accuracy is Alcator C-Mod ($0.05/\beta_p$), ASDEX (15%), ASDEX Upgrade (10%), DIII-D ($0.05/\beta_p$), JET (12%), JFT-2M (15%), JT-60U (Na), PBX-M (15%).

62. **BEPMHD:** Poloidal beta computed from the MHD equilibrium fit.
Normal level of accuracy is Alcator C-Mod ($0.05\ \beta_p$), ASDEX (15%), ASDEX Upgrade (10%), DIII-D ($0.05\ \beta_p$), JET (Na), JFT-2M (15%), JT-60U (Na), PBX-M (20%).

63. **BETMHD:** Toroidal beta computed from the MHD equilibrium fit.
Normal level of accuracy is Alcator C-Mod ($0.05/\beta_p$), ASDEX (18%), ASDEX Upgrade (Na), DIII-D ($0.05/\beta_p$), JET (12%), JFT-2M (15%), JT-60U (Na), PBX-M (20%).

64. **BEPDIA:** Corrected poloidal diamagnetic beta from diamagnetic coils (15%).
Normal level of accuracy is Alcator C-Mod (0.05), ASDEX (15%), ASDEX Upgrade (10%), JT-60U (5%), DIII-D, JET, JFT-2M, PBX-M: Na.

65. **BMHDMDIA:** Offset for ASDEX between diamagnetic beta poloidal and MHD beta poloidal during the Ohmic phase, (5%).
Other devices: Na.

Density

66. NEL: Central line average electron density in m^{-3} from the interferometer.
Normal level of accuracy is Alcator C-Mod (Na), ASDEX (2%), ASDEX Upgrade (3%), DIII-D (2×10^{18} m^{-3}), JET (8%), JFT-2M (2%), JT-60U (10%), PBX-M (5%).

67. DNELDT: The time rate of change of NEL in m^{-3}/s.
Normal level of accuracy is similar to NEL.

68. NEV: The volume averaged electron density in m^{-3}.
Alcator C-Mod (Na)
ASDEX: Determined from 4 HCN interferometry channels fitting $n(x) = n(1) + (n(0) - n(1))\ (1 - x^{\alpha})\beta$, $0 \leq x \leq 1$, (5%) For all volume integrations (NEV, TEV, WEKIN), a circular plasma was assumed.
ASDEX Upgrade (Na)
DIII-D: Determined by a spline density profile fit to the CO_2 and Thomson scattering density data (10%).
JET: Determined from weighted summation over 6 interferometer channels (10%).
JFT-2M: Determined from an analytic fit with fixed profile shape to 2 interferometer channels (30%).
JT-60U (Na)
PBX-M: (Na).

69. NE0: The central electron density at the magnetic axis in m^{-3} determined in same manner as NEV.
Normal level of accuracy is Alcator C-Mod (Na), ASDEX (10%), ASDEX Upgrade (Na), DIII-D (15%), JET (10%), JFT-2M (Na), JT-60U (Na), PBX-M (Na).

70. NE95: The electron density at R95.
Normal level of accuracy is Alcator C-Mod (Na), ASDEX (Na), ASDEX Upgrade (Na), DIII-D (30%), JET (30-40%), JFT-2M (Na), JT-60U (Na), PBX-M (Na).

Impurities

71. ZEFF: Line average plasma effective charge determined from visible bremsstrahlung. Normal level of accuracy is Alcator C-Mod (20%), ASDEX (10%), ASDEX Upgrade (Na), DIII-D (20%), JET (30%). JFT-2M, JT-60U (Na), PBX-M: Na.

72. PRAD: Total radiated power in watts as measured by bolometer.

Normal level of accuracy is Alcator C-Mod (20%), ASDEX (20%), ASDEX Upgrade (20%), DIII-D (15%), JET (10-15%), JFT-2M (10-20%), JT-60U (20%), PBX-M (25%).

73. **PRADE** Total radiated power outside the plasma in watts.
Normal level of accuracy is Alcator C-Mod (20%), ASDEX (10%), ASDEX Upgrade (Na), DIII-D (20%), JET (10%), JFT-2M (Na), JT-60U (Na), PBX-M (Na).

Input Powers

74. **POHM:** Total Ohmic power in watts.
Alcator C-Mod: VSURF × IP (15%)
ASDEX: Determined from Max {0, VSURF × IP}, (Ohmic: ± 5% H: 50%).
ASDEX Upgrade : VSURF × IP (15%)
DIII-D: Calculated using $CB_{10}I_p^2RGEO^2/(W_Tn_e)$. B_{10} is the central visible bremsstrahlung signal. When n_e is determined from the radial (vertical) CO_2 chord, C is equal to 1.03×10^{-19} (9.92×10^{-20}) (15%).
JET: Corrected for inductance effects (20%).
JFT-2M: Calculated as VSURF × IP (10%).
JT-60U: VSURF × IP (20%)
PBX-M: Calculated as VSURF × IP (50%).

75. **ENBI:** Neutral beam energy weighted by power in volts. This quantity is calculated from $\Sigma E_iP_i/\Sigma P_i$ where E_i is the beam energy and P_i is the beam power for source i. For ASDEX the primary energy component is given.
Normal level of accuracy is Alcator C-Mod (Na), ASDEX (0.2 KV), ASDEX Upgrade (5%), DIII-D (10%), JET (12%), JFT-2M (Na), JT-60U (5%), PBX-M (Na).

76. **PINJ:** The injected neutral beam power with beam of (BGASA, BGASZ) that passes into the torus in watts. Zero if no beams are on. The total injected power is PINJ + PINJ2 + PINJ3.
Normal level of accuracy for this variable is Alcator C-Mod (Na), ASDEX (10%), ASDEX Upgrade (5%), DIII-D (10%), JET (6%), JFT-2M (5%), JT-60U (5%), PBX-M (5%).

77. **BSOURCE:** The power fractions injected by neutral beam e.g. P1 = 80%, P2 = 10% and P3 = 10% then BSOURCE = 801010.

78. **PINJ2:** The injected neutral beam power from a second source with beam of (BGASA2, BGASZ2) in watts (JET only). Zero if no beams of second source are on.
Normal level of accuracy is JET (6%). Other devices: Na.

79. **BSOURCE2:** The power fractions injected by neutral beam with the second source (JET only). For 89-92 data the possibilities for BSOURCE and BSOURCE2 are 712306 for 60 kV H^o, 393031 for 100 kV H^o, 781606 for 80 kV D^o, 652114 for 140 kV D^o, 990000 for ^3He or ^4He beams).

80. **PINJ3:** The injected neutral beam power from Tritium PINI's in watts. Normal level of accuracy is JET (6%). Other devices: Na.

81. **BSOURCE3:** The power fractions injected by neutral beam tritium PINI's (JET only). BSOURCE3 = 781606 for 1% Tritium or BSOURCE3 = 791209 for 100% Tritium.

82. **COCTR:** Fraction of beam power co-injected as compared to the total beam power injected.

83. **PABS:** Total injected neutral beam power minus shine through in watts. Zero if no beams are on.
Normal level of accuracy is Alcator C-Mod (Na), ASDEX (10%), ASDEX Upgrade (10%), DIII-D (10%), JET (10%), JFT-2M (< 10%), JT-60U (10%), PBX-M (10%).

84. **PFLOSS:** Amount of neutral beam power in watts that is lost from the plasma through charge exchange and unconfined orbits.
Alcator C-Mod: (Na)
ASDEX: From fits to FREYA code results, (30%).
ASDEX Upgrade (Na)
DIII-D: PNBI exp (3.3 - IP/10^6/100(30 %).
JET: (ΣPINJ) exp (3.35 - 0.667 |IP| /10^6 - 0.2 NEL/10^{19})/100 (30%).
JFT-2M: From fits to Monte Carlo code results (20%).
JT-60U: (Na)
PBX-M: From fits to the TRANSP code results (20%).

85. **ECHFREQ:** ECH frequency in Hz.

86. **ECHMODE:** Mode of ECH waves; O is ordinary, X is extraordinary.

87. **ECHLOC:** Location of ECH launch, IN identifies waves launched from the high field side or inside of the vessel, and OUT is from the low field side.

88. **PECH:** Total absorbed ECH power in Watts. Zero if no ECH is applied.
Normal level of accuracy is ASDEX Upgrade (10%), DIII-D (10%).
Other devices: Na.

89. **ICFREQ:** Frequency of ICRH waves in Hz.

90. **ICSCHEME:** ICRH heating scheme. Possible values: HMIN for H-minority, HE3MIN for ^3He-minority, or H2NDHARM for second harmonic H-heating.

91. **ICANTEN:** Antenna phasing. Possible values are DIPOLE or MONOPOLE.

92. ICLOC: Location of ICRF antenna. Possible values are IN (high field side) or OUT (low field side).

93. PICRH: The absorbed ICRH power with frequency ICFREQ in Watts. Zero if no ICRH is applied.
Normal level of accuracy is ASDEX Upgrade (10%), JET (10%).
Other devices: Na.

94. ICFREQ2: Second frequency of ICRH waves in Hz.

95. ICSCHEM2: ICRH heating scheme for second frequency. Possible values: HMIN for H-minority, HE3MIN for ^{3}He - minority, or H2NDHARM for second harmonic H-heating.

96. ICANTEN2: Antenna phasing for second frequency. Possible values are DIPOLE or MONOPOLE.

97. ICLOC2: Location of ICRF antenna for second frequency. Possible values are IN (high field side) or OUT (low field side).

98. PICRH2: The absorbed ICRH power with frequency ICFREQ2 in Watts. Zero if no ICRH with ICFREQ2 is applied.
Normal level of accuracy is JET (10%).
Other devices: Na.

99. LHFREQ: LH frequency in Hz.

100. LHNPAR: Peak $n_{||}$ of LH waves.

101. PLH: The absorbed LH power with frequency LHFREQ in watts. Zero if no LH is applied.
Normal level of accuracy is JET (10%). Other devices: Na.

102. LHFREQ 2: The frequency of a second LH source in Hz.

103. LHNPAR 2: The peak $n_{||}$ of a second LH wave.

104 PLH2: The absorbed LH power from a second LH source in watts. Zero if no LH of second source is applied.

105. IBFREQ: The frequency of the Ion Bernstein wave heating.

106 PIBW: Total Ion Bernstein Wave heating power. Zero if no IBW is applied.

107. DWDIA: Time rate of change of the total plasma stored energy as determined by the diamagnetic loop in watts.
Alcator C-Mod: (20%)
ASDEX: Parabolic fit to time evolution of diamagnetic beta β_p over ± 6 ms when DWHC = 0 (20%). Set by hand from

drawing the tangent to the WDIA time trace when DWHC = 1.
JET: Running average method over ± 100 ms (10%).
JFT-2M: Simple derivative over ± 5 ms (20 %).
JT-60U: (20%)
ASDEX Upgrade, DIII-D, PBX-M: Na.

108. DWDIAPAR: Time derivative for ASDEX of Wdia from a parabolic fit to the three available H-mode points.
Normal level of accuracy is ASDEX (20%). Other devices: Na.

109. DWMHD: Time rate of change of the total plasma stored energy as determined from MHD in watts.
Alcator C-Mod: (20%)
ASDEX: As for DWDIA (20%).
ASDEX Upgrade: (Na)
DIII-D: A spline fit is made to W and this fitted curve is then differentiated (25%).
JET: As for DWDIA (20%).
JFT-2M: As for DWDIA (20%).
JT-60U: (Na)
PBX-M: (10%).

110. DWHC: = 1 when DWDIA and DWMHD have been corrected by hand for ASDEX.

Temperatures

111. TEV: The volume averaged electron temperature eV.
ASDEX: From 16 radial YAG measurements fitting $T_e(x) = T_e(0) \exp(ax^2 + bx^4 + cx^6)$, (5%).
DIII-D: Determined by a spline temperature profile fit to the Thomson scattering data (10%).
JET: From 51 point ECE temperature profile (10%).
JFT-2M: Na.
PBX-M: Volume averaged electron temperature computed from BETMHD, VOL, NEL, assuming $Z_{eff} = 1$ (30%).
Other devices: Na

112. TE0: The electron temperature at the magnetic axis in eV.
ASDEX: From 16 radial YAG measurements under the same profile assumptions as for TEV (10%).
DIII-D: Determined by a spline temperature profile fit to the Thomson scattering data (10%).
JET: From ECE temperature profile (10%).
Other devices: Na

113. TE95: The electron temperature at R95 in eV.
Normal level of accuracy is ASDEX (50-100%), DIII-D (30%), JET (50%), Other devices: Na

114. TIV: The volume averaged ion temperature in eV.

DIII-D: Determined by a spline temperature profile fit to the charge exchange recombination data (10%).

JET: Estimated from TIV = TI0 × TEV/TE0 (30%).

PBX-M: TIV = TEV (30%).

Other devices: Na.

115. TI0: The ion temperature at the magnetic axis in eV.

Alcator C-Mod: (15%)

DIII-D: Determined by a spline temperature profile fit to the charge exchange recombination data (10%).

JET: From Crystal X-ray diagnostic (10%).

Other devices: Na.

116. TI95: The ion temperature at R95 in eV.

Normal level of accuracy is DIII-D (30%), JET (50-100%).

Other devices: Na

Energies

117. WDIA: Total plasma energies in joules as determined from the diamagnetic loop.

ASDEX: Diamagnetic energy, $0.471 R_{geo}\ 10^{-6} Ip^2 \beta_p$ (dia), (ohmic: 20%, H: 10%).

JFT-2M: In Ohmic WDIA = $W_{DIA}^{measured}$ (± 1-2 kJ).

In H-mode phase WDIA = $W_{DIA}^{measured}$ - ΔW, where

ΔW = $W_{DIA}^{measured}$ (ohmic) - WMHD (ohmic).

Normal level of accuracy is Alcator C-Mod (+10 kJ -30 kJ), ASDEX Upgrade (10%), DIII-D ($0.1/\beta_p$), JET (5%), JFT-2M (15%). JT-60U (5%), PBX-M: Na.

118. WMHD: Total plasma energy in joules as determined by a MHD equilibrium fit.

ASDEX: MHD energy, $4.71 \times 10^{-6} R_{geo} I_p^2 \beta_p$ (mhd), (ohmic: 20%, H: 10%).

Normal level of accuracy is Alcator C-Mod ($0.05/\beta_p$), ASDEX Upgrade (10%), DIII-D ($0.05/\beta_p$), JET (15%), JFT-2M (15%), JT-60U (Na), PBX-M (15%).

119. WKIN: Total thermal plasma energy in joules as determined from kinetic measurements.

ASDEX: WEKIN (1 + (7-Zeff)/(7-1)) (25%).

DIII-D: Normal level of accuracy is $0.05/\beta_p$.

JET: From a profile fit assuming flat Z_{eff} profile and T_i profile as T_e (25%).

Other devices: Na.

120. WEKIN: Total thermal electron plasma energy in joules as determined from kinetic measurements.
Normal level of accuracy is ASDEX (10%, H: 15%) DIII-D (15%), JET (20%). Other devices: Na.

121. WIKIN: Total thermal ion plasma energy in joules as determined from kinetic measurements.
DIII-D: Error 15%.
JET: From ECE temperature profile shape normalised to Ti(o) from crystal X-ray diagnostic (15%).
Other devices: Na.

122. WFPER: Total perpendicular fast ion due to NBI energy in joules as determined from transport calculations.
JET: Calculated from the PENCIL code (30%).
JFT-2M: From Monte Carlo code (20%).
PBX-M: From TRANSP runs (30%).
Other devices: Na.

123. WFPAR: Total parallel fast ion energy due to NBI in joules as determined from transport calculations.
JET: Calculated from the PENCIL code (30%).
JFT-2M: From Monte Carlo code (20%).
PBX-M: From TRANSP runs (30%).
Other devices: Na.

124. WFFORM: Total fast ion energy due to NBI in joules estimated from approximate formula. Zero if no NBI.
ASDEX: C_j NEL$^{-1.25}$ PINJ$^{0.95}$ ENBI$^{0.75}$ WTH$^{0.5}$, where WTH = WDIA - 1.5 WFFORM × WFANI. (Implicit equation for WFFORM solved numerically by a bisection method). $C_j = 7.05 \times 10^{10}$ (D° → D); 3.10×10^{10} (H° → D).
DIII-D

$$\frac{0.55 P_b \tau_{se}}{2}\left\{1+\frac{2}{3}\left(\frac{v_c}{v_b}\right)^2\left\{\frac{1}{2}\ln\left[\frac{(v_b+v_c)^2}{v_b^2-v_b v_c+v_c^2}\right]-\sqrt{3}\left[\frac{\pi}{6}+\tan^{-1}\left(\frac{2v_b-v_c}{\sqrt{3}v_c}\right)\right]\right\}\right\}$$

The velocities v_c and v_b are determined from the critical energy and the beam energy respectively, and P_b is the injected neutral beam power. The quantity τ_{se} is the slowing down-time on electrons first defined by Spitzer, $\tau_{se} = 6.3 \times 10^8 \frac{A_b T_e^{3/2}}{Z_b^2 n_e \ln \Lambda_e}$,

where A_b and Z_b are the atomic mass and charge of the fast ions, T_e is the electron temperature in eV, n_e is the electron density in cm^{-3},

and ln $\Lambda_e \simeq 16$ is the Coulomb logarithm. If ion drag were negligible, the term in the brackets would be identically one. For DIII-D parameters, however, this term varies rapidly with temperature. To give better agreement with ONETWO results, the above formula is multiplied by 0.55.

JET: 0.16×10^{19} PINJ/NEV for SHOT $\leq$ 18760;
10^{19} (0.16 P_{80kV} + 0.3 P_{140kV} + 0.02 P_{He})/NEV for SHOT > 18760.
JFT-2M: WFPER + WFPAR.
PBX-M: WFPER + WFPAR.
PDX: WFPER + WFPAR.
Normal level of accuracy is ASDEX (30%), DIII-D (50%), JET (50%), JFT-2M (20%). Other devices: Na.

125. WFANI: Estimate of fraction of perpendicular fast ion energy as compared to the total fast ion energy due to NBI (± 50%).
If WFPER and WFPAR are available WFANI = WFPER/(WFPER + WFPAR). otherwise:

ASDEX: 2.8×10^{-3} $NEL^{0.15}/ENBI^{0.14}$ ($D^\circ \rightarrow D$);
112 $NEL^{-0.12}$ ($H^\circ \rightarrow D$).
DIII-D: The fast ion anisotropy is calculated only from geometry; the angles of the beam center line are known relative to the geometric axis of the tokamak and from this the perpendicular and parallel components can be determined.
JET: Set to missing.
Normal level of accuracy is ASDEX (15%), DIII-D (50%), JET (50%), JFT-2M (30%). Other devices: Na.

126 WFICRH: Estimate of the perpendicular fast ion energy content due to ICRH heating in Joules.
JET: Estimated with the PION code.
Zero if no ICRH is applied.
Normal level of accuracy is JET (50%). Other devices: Na.

127. WFICRHP: Estimate of the parallel fast ion energy content due to ICRH heating in Joules.
JET: Estimated with the PION code.
Zero if no ICRH is applied.
Normal level of accuracy is JET (50%).
Other devices: Na.

128. WFANIIC: Estimate of fraction of perpendicular fast ion energy compared to the total fast ion energy due to ICRH heating.
Normal level of accuracy is JET (50%).
Other devices: Na.

Energy Confinement Times

129. TAUDIA: Total diamagnetic energy confinement time (WDIA/(POHM + PABS + P_{RF} - DWDIA)) in seconds. (P_{RF} = any RF heating)

Normal level of accuracy is Alcator C-Mod (15%), ASDEX (ohmic 25%, H 15%), ASDEX Upgrade (15%), DIII-D (15%), JET (25% for ohmic, 10% for H-mode), JFT-2M (20%), JT-60U (10%), PBX-M (Na).

130. TAUMHD: Total MHD energy confinement time (WMHD/(POHM + PABS + P_{RF} - DWMHD) in seconds. (P_{RF} = any RF heating)
Normal level of accuracy is Alcator C-Mod (15%), ASDEX (H 15%), ASDEX Upgrade (15%), DIII-D (15%), JET (35%), JFT-2M (20%), JT-60U (Na), PBX-M (20%).

131. TAUTH1: Thermal energy confinement time (WKIN/(POHM + PABS-DWMHD-PFLOSS)) in seconds.
Normal level of accuracy is ASDEX (25%), DIII-D (25%), JET (35%). , Other devices: Na.

132. TAUTH2: Thermal energy confinement time (WMHD-WFFORM)/(POHM + PABS - DWMHD - PFLOSS)) in seconds. For both PBX-M and PDX, $3/4W_{f\perp} + 3/2W_{f\parallel}$ was used instead of WFFORM.
Normal level of accuracy is ASDEX (30%), DIII-D (Na), JET (30%), JFT-2M (25%), PBX-M (30%). Other devices: Na

133. THTIME: The fast ion thermalisation time in seconds (NBI only).

$$\text{THTIME} \triangleq \frac{\tau_S}{3} \ln\left\{1 + \left(\frac{\text{ENBI}}{E_c}\right)^{3/2}\right\}$$

$$\tau_s = 1.17 \times 10^{18} \left(\frac{\text{BGASA}}{\text{BGASZ}^2}\right)\left(\frac{\text{TEV}}{10^3}\right)^{3/2} \frac{1}{\text{NEV}}$$

$$E_C = 14.8\ \text{BGASA} \left(\frac{\text{PGASZ}}{\text{PGASA}}\right)^{2/3} \text{TEV}$$

Normal level of accuracy is 30% to 50% when available.

Extra Information

134. DALFMP: D_α emission on the mid-plane. Alcator C-Mod (30%).

135. DALFRAT: Ratio of D_α emission in the divertor to D_α emission on the mid-plane.
Normal level of accuracy is Alcator C-Mod (30%). Other devices: Na

136 TAUP An estimate of the particle confinement time.
For Alcator C-Mod : TAUP= VOL*NEV/(g*SPLASMA)
with g=15*4*π*0.529/1.6e-16*averaged Hα emission
(averaged Hα emission in mW/ster cm^2). This formula underestimates the particle confinement time but is useful to

compare conditions of different discharges. Normal level of accuracy is (40%). Other devices: Na.

137. PMAIN: Neutral pressure in the main chamber in Pascals. Normal level of accuracy is (40%).

138. PDIV: Neutral pressure in the divertor region in Pascals. Normal level of accuracy is (40%).

139. BIASM: Divertor bias scheme. m=0 mode (BIASM=0) in which the divertor plates are biased with respect to the vessel.
m=1 mode (BIASM=1) in which the divertor plates are biased with respect to each other.

140 VBIAS: Divertor or limiter bias voltage in volts.
For the m=0 mode: bias voltage of the divertor plates with respect to the vessel;
For the m=1 mode: bias voltage of the inner plate with respect to the outer plate.

141. VTO95: Toroidal rotation velocity at R95 in m/sec. Positive velocity in the co-direction.

142. VPO95: Poloidal rotation velocity at R95 in m/sec. Positive velocity in the ion diamagnetic direction.

143. SELDB1 Flag for the selection criteria of the standard dataset (first flag for DB1).

$SELDB1 = \sum_{n=1}^{10} a(I.n) \times 10^{n-1}$ (SELDB1 = 1111111111 when all criteria are fulfilled).

I.1 Single-null configuration with ion gradB toward X-point (all the devices, except PBX-M)
a(I.1)=0
if IGRADB = 1 and CONGIF = 1 then a(I.1) = 1
if TOK = PBX-M then a(I.1) = 1

I.2 Deuterium plasma (all the devices)
a(I.2)=0
if PGASA = 2 and $1 \leq$ BGASAi ≤ 2 then a(I.2) = 1

I.3 Avoid increased threshold at low density (each device)
a(I.3)=0
if NEL $\geq$ NELmin then a(I.3) = 1 (NELmin for each device)

I.4 Avoid increased threshold at low Q95 (each device)
a(I.4)=0
if Q95 $\geq$ Q95min then a(I.4) = 1 (Q95min for each device)

I.5 Avoid time points too close to beginning of heat pulse (each device)
a(I.5)=0
if TIME - AUXTIME ≥ delaymin then a(I.5) = 1 (delaymin for each device such that the data are useful, guide line: delaymin = 0.25 TAUE)

I.6 Avoid particular effects due to ctr-NBI (all the devices)
a(I.6)=0
if COCTR ≥ 0.2 then a(I.6) = 1

I.7 Avoid increased threshold due to small distance to in-vessel components
a(I.7)=0
if plasma "far enough" from wall then a(I.7) = 1 ("far enough" defined by a condition on GAPx or/and SEPLIM for each device)
For ASDEX: GAPOUT ≥ 0.025 m
For AUG: GAPOUT ≥ 0.025 m
FOR JFT-2M: GAPOUT ≥ 0.02 m

I.8 Avoid tangential NBI in PBX-M
a(I.8)=1
if WFANI ≤ 0.5 and TOK = PBX-M then a(I.8) = 0

I.9 Avoid high radiation losses (for each device)
a(I.9)=1
if PRAD ≥ PRADmax then a(I.8) = 0 (PRADmax for each device)

I.10 Avoid other effects preventing the H-mode and works as a marker for outliers.
a(I.10)=1
if H-Mode prevented by another identified cause,
then a(I.10) = 0
if H-Mode prevented by a non-identified phenomenon (outliers)
then a(I.10) = 9

APPENDIX 2

Reduced variable list

TOK, UPDATE , SHOT, TIME, LHTIME, PHASE, PGASA, RGEO, AMIN, KAPPA, CONFIG, IGRADB, EVAP, BT, IP, Q95, NEL, POHM, SELDB1,
and in addition if auxiliary heating used:
AUXHEAT, ONTIME, AUXTIME
and also : Power and characteristics of the used auxiliary heating such as BGASAi for NBI, resonance position and mode for RF-heating, etc.

APPENDIX 3

Access to the threshold database via FTP and to the review sheets of Alcator C-Mod with the World Wide Web.

The threshold database is accessible with FTP from the server at IPP-Garching, in the directory /ftp/pub/iter/world.

The server name is: ftp.ipp-garching.mpg.de

The access is given by the following commands.

ftp ftp.ipp-garching.mpg.de
user: iter
password: iter-eda
cd world

The review sheets from Alcator C-Mod are available at MIT via World Wide Web:

http://CMod2.pfc.mit.edv/~g/CMod_iterdb_LH.htmL

The review sheets from ASDEX Upgrade will soon be available at IPP-Garching on World Wide Web.